Design strategies for rechargeable aqueous metal-ion batteries

Yang Li[1†], Xin Zhao[1†], Yifu Gao[1], Yichen Ding[1], Zhichun Si[1], Liubing Dong[2], Dong Zhou[1*] & Feiyu Kang[1*]

[1]*Tsinghua Shenzhen International Graduate School, Tsinghua University, Shenzhen 518055, China;*
[2]*College of Chemistry and Materials Science, Jinan University, Guangzhou 511443, China*

Rechargeable aqueous metal-ion batteries (AMBs) have attracted extensive scientific and commercial interest due to their potential for cost-effective, highly safe, and scalable stationary energy storage. However, their limited output voltage, inadequate energy density, and poor reversibility of ambiguous electrode reactions in aqueous electrolytes strongly limit their practical viability. This review aims to elucidate the challenges of existing AMBs from the material design to whole device applications. We summarize the emerging electrochemistry, fundamental properties, and key issues in interfacial behaviors of various classes of prevailing AMBs, including aqueous alkali metal-ion batteries and multivalent-ion batteries, and present an appraisal of recent advances for addressing the performance deficiency. Specifically, the progress of zinc-ion batteries is highlighted to provide a ubiquitous guideline for their commercialization in the grid-scale energy storage. Finally, we figure out the dominating general challenges for achieving high-performance AMBs, laying out a perspective for future breakthroughs.

aqueous metal-ion batteries, aqueous alkali metal-ion batteries, zinc-ion batteries, interfacial behavior, stationary energy storage

1   Introduction

To achieve the strategic goal of "carbon peak" and "carbon neutrality", it is imminent to develop green renewable energy [1–3]. The pumped storage and other physical energy storage techniques, such as solar and wind energy, are intermittent and regional, putting forward a higher demand for advanced grid-scale energy storage devices [4]. With the merits of high energy density, long cycle life and low self-discharge, lithium-ion batteries (LIB) based on organic liquid electrolytes have been widely used in the field of portable electronic equipment since their discovery in 1976 [5]. However, the high cost and safety problems seriously restrict their appli-

cation in the stationary energy storage. Therefore, it is of great significance to develop novel cost-effective and highly safe electrochemical energy storage systems [6,7].

Compared with traditional LIBs, aqueous metal-ion batteries (AMBs) possess the following incomparable superiorities. (1) Cost effectiveness. The argument for the low cost originates from three factors: easy-accessible raw materials, minimal requirements for manufacturing procedures, and limited demand for the battery protection and management systems. The use of low-cost aqueous electrolyte and electrode materials can not only reduce the expense of raw materials, but also decrease the manufacture inputs giving those aqueous batteries that can be assembled in the atmospheric environment [8,9]. Due to their reliability, the expenditure on the maintenance also goes down. (2) Environmental friendliness. Water is selected as an electrolyte solvent in AMBs, which possesses the characteristics of non-toxicity and not

volatility. (3) High safety. The non-flammable nature of aqueous electrolytes can guarantee a safe operation even under extreme conditions. (4) Reliability in the large-scale energy storage. The existence of a water medium improves the ionic conductivity of electrolytes, which endows a faster charging–discharging ability of AMBs [10]. Meanwhile, the improved possibility of thicker electrode manufactures increases energy density ultimately.

The main progress of AMBs is summarized in Figure 1a. Their development is astounding since Gaston Planté elucidated the concept of a lead–acid battery in 1859 [11]. After that, researchers pursued corrosion-resistant collectors and simplified the fabrication procedure to promote their commercialization. Up to now, lead–acid batteries have played a significant role in energy storage devices continuously [12]. However, the low energy density of lead–acid batteries (~30 Wh kg^{-1}) is a major obstacle that confines their further development [13]. With the target to improve the energy density, alkaline rechargeable ABs were invented twenty years later. Owing to the merits of suitable redox potential, high reversibility and fairly high specific capacity, alkaline AMBs soon occupied the market ranging from heavy-duty industrial applications to portable electronic instruments. Among them, Ni–Cd batteries were phased out due to the toxicity and stagnating energy density (~35 Wh kg^{-1}) [14].

Practically, the fluctuation of pH has a direct and significant impact on the electrochemical performance of AMBs [15]. For instance, lead–acid batteries, which use low pH acidic electrolytes, usually suffer from hydrogen evolution reaction (HER) at the anode together with the low Coulombic efficiency (CE) by the corrosion and by-product formation [11]. On the other hand, Ni-based (Ni–Cd, Ni–

metal hydride (Ni–MH), *etc.*) and alkaline Zn–MnO$_2$ batteries, which use KOH as the alkaline electrolyte, undergo the dendrite formation and uneven electric field in bulk. Oxygen evolution reaction further reduces the reaction kinetics at the cathode, leading to serious capacity attenuation of AMBs [16–18]. Therefore, researchers have drawn their attention to the near-neutral electrolyte system.

Depending on the valence states of different metal carries, AMBs can be divided into two categories: aqueous alkali metal-ion batteries (including aqueous LIBs, aqueous sodium-ion batteries (SIBs), and aqueous potassium-ion batteries (PIBs)) and aqueous multivalent-ion batteries (including aqueous zinc-ion batteries (ZIBs), aqueous calcium-ion batteries (CIBs), aqueous magnesium-ion batteries (MIBs) and aqueous aluminium-ion batteries (AIBs)). Aqueous LIBs have been preferentially developed based on the background of conventional organic LIBs. In 1994, Dahn *et al.* [19] proposed the first aqueous LIB which was composed of the VO$_2$ anode and LiMn$_2$O$_4$ cathode in the LiNO$_3$ electrolyte. The as-prepared LIB exhibited an operating voltage of 1.5 V, corresponding to an energy density of ~55 Wh kg^{-1}. Nevertheless, the cyclability of such a LIB was far from satisfaction. Considering the insufficient reserve of lithium element in the earth's crust, aqueous SIBs and PIBs are more attractive for the large-scale energy storage due to the crustal abundance of Na and K. Nevertheless, few compounds can be matched with Na$^+$ and K$^+$ as electrode materials due to their large cation radius (Figure 1b). Compared with alkali metal ions, multivalent metal ions (Zn^{2+}, Ca^{2+}, Mg^{2+}, Al^{3+}, *etc.*) as carriers can transfer more than one electron and provide a higher capacity under the condition of equivalent embedding sites, which facilitates the breaking
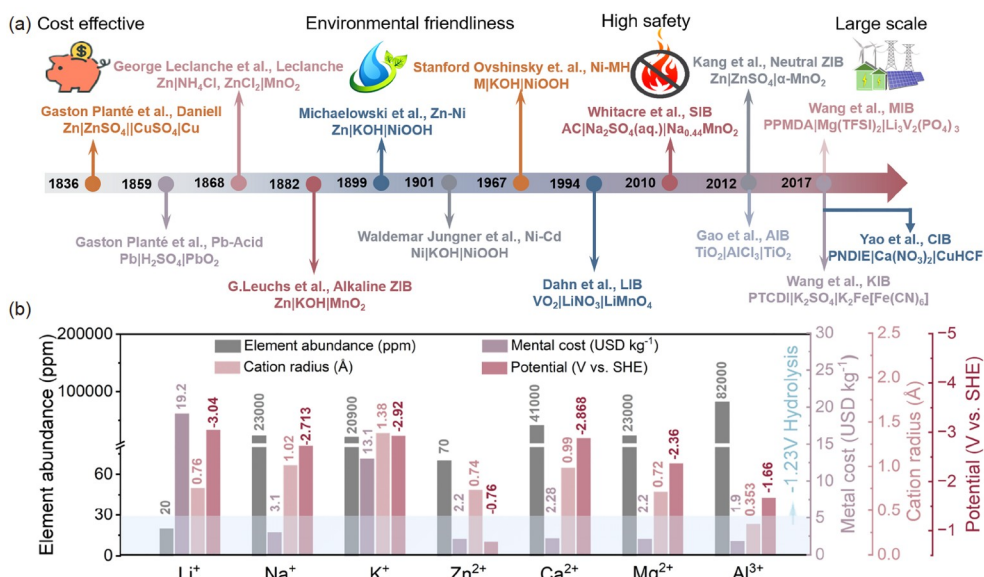

Figure 1 Summary of main progress and advantages of AMBs. (a) Timeline for the development of AMBs. (b) Comparison of element abundance, metal cost, cation radius and potential of the typical metal-ion carriers (color online).

through the limitation of energy density [20,21]. Meanwhile, such multivalent metal ions are earth-abundant and accessible (Figure 1b). Especially, the concept of neutral ZIBs was first proposed by Kang *et al.* [22] in 2012, which are combined with the Zn foil anode and α-MnO$_2$ cathode in the ZnSO$_4$ electrolyte. The Zn anode possesses a high theoretical volumetric capacity (5,855 mAh cm^{-3}) and gravimetric capacity (820 mAh g^{-1}). The standard reduction potential of Zn/Zn^{2+} was calculated to be −0.76 V *vs.* standard hydrogen electrode (SHE), enabling ZIBs to work steadily in aqueous electrolytes [23,24]. The moderate ionic radius of Zn^{2+} and relatively low cost of Zn further promote the development of ZIBs as the most promising aqueous multivalent-ion battery system. By contrast, the research progress of aqueous CIBs, MIBs and AIBs is still stagnant due to the inappropriate redox potential.

In this review, we present a systematic overview of the recent advances of diverse AMBs, including aqueous alkali metal-ion batteries and multivalent-ion batteries, from the perspectives of electrochemical mechanisms, basic properties, and the interfacial behaviors including the hydrogen evolution and corrosion caused by the presence of water media. We also present the remaining challenges of AMBs and provide a roadmap starting with the material design and ending with whole device applications.

2   Aqueous alkali metal-ion batteries

2.1   Aqueous Li-ion batteries

Transforming LIBs from traditional organic electrolytes to aqueous electrolytes offers advantages such as non-flammability, low viscosity, high ionic conductivity, eco-friendliness and low cost [25]. However, the much narrower electrochemical stability window of dilute aqueous electrolytes (~1.23 V) greatly constrains the energy density of aqueous LIBs to less than 70 Wh kg^{-1} [26]. Furthermore, such an issue limits the anode option to only a few electrodes with relatively high voltage (Figure 2a) [26]. Luckily, the water-in-salt electrolyte (WISE), first proposed in 2015, posed a step large forward in the progress of aqueous LIBs [27]. In the reported super-concentrated electrolyte (lithium *bis*(trifluoromethanesulphonyl)imide (LiTFSI) with a molality of 21 mol L^{-1}), the ratio of water and lithium ions dropped to ~2.7, thus eliminating most of the free water molecules in the electrolyte system (Figure 2b). Such a strategy has been demonstrated to significantly reduce the electrochemical activity of water; as a result, a solid-electrolyte interphase (SEI) mainly composed of the reduction products of anions was developed, and the electrochemical stability window was successfully expanded to ~3.0 V (Figure 2c). Moreover, a Mo$_6$S$_8$|LiMn$_2$O$_4$ cell with the WISE demonstrated a remarkable improvement in capacity reten-
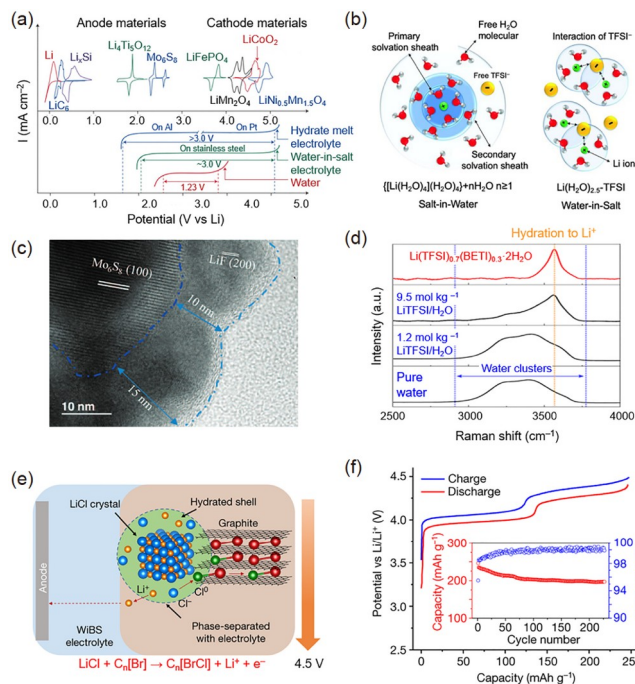

Figure 2   WISE for aqueous LIBs. (a) Electrochemical stability windows of representative aqueous electrolytes, and redox potentials of electrode materials [26]. (b) Illustration of the evolution of the Li$^+$ primary solvation sheath in diluted and WISE solutions [27]. (c) TEM images of cycled Mo$_6$S$_8$ [27]. (d) Raman spectra of Li(TFSI)$_{0.7}$(BETI)$_{0.3}$·2H$_2$O electrolyte compared with those of organic Li salt-based aqueous solutions, namely, dilute 1.2 mol kg^{-1} LiTFSI/H$_2$O and concentrated 9.5 mol kg^{-1} LiTFSI/H$_2$O [29]. (e) Schematic of the conversion–intercalation mechanism occurring in the graphite composite cathode during its oxidation in the WiBS aqueous-gel electrolyte [30]. (f) Galvanostatic charge/discharge profiles of the graphite composite cathode at a current density of 80 mA g^{-1}. Inset: discharge capacity retention and CE [30] (color online).

tion (68% with 1000 cycles), average discharge voltage (1.8 V), and energy density (100 Wh kg^{-1}). Another approach was to develop WISE with binary salts. It is demonstrated that the electrolyte containing 21 mol L^{-1} LiTFSI and 7 mol L^{-1} lithium triflate (LiOTf) could obtain a broader window (4.9 V *vs.* Li/Li$^+$) [28]. This system allowed for the use of TiO$_2$ as the anode material and provided a TiO$_2$|LiMn$_2$O$_4$ cell with a high discharge voltage of 2.1 V and an energy density of 100 Wh kg^{-1}. Moreover, a Li(TFSI)$_{0.7}$-(BETI)$_{0.3}$·2H$_2$O hydrate-melt electrolyte was proposed by dissolving LiTFSI and LiN(SO$_2$C$_2$F$_5$)$_2$ (LiBETI) salts in water (Figure 2d), in which all water molecules are coordinated with lithium ions [29]. Such an electrolyte demonstrated an electrochemical window of ~2.7 V, enabling the utilization of a commercially-available Li$_4$Ti$_5$O$_{12}$ anode. The resultant Li$_4$Ti$_5$O$_{12}$|LiCoO$_2$ or Li$_4$Ti$_5$O$_{12}$|LiNi$_{0.5}$Mn$_{1.5}$O$_4$ full cells possessed a high capacity of ~45 Ah kg^{-1} at 10 C and ~25 Ah kg^{-1} at 6.8 C, respectively.

To further increase the energy density of aqueous LIBs, electrode chemistry has been explored from the intercalation type to the conversion type. For example, a two-step halogen

conversion–intercalation chemistry was proven to happen in graphite containing equimolar lithium halide salts (*e.g.*, $(LiBr)_{0.5}(LiCl)_{0.5}$–graphite) [30]. It is demonstrated that Br^- was firstly oxidized to Br^0 before its intercalation into graphite forming $C_n[Br]$ at 4.0–4.2 V *vs.* Li^+/Li. Then the oxidation of Cl^- and the intercalation of Cl^0 started when the cell was further charged to 4.5 V (Figure 2e). The aforementioned mechanism demonstrated the outstanding reversibility, as evidenced by the two corresponding plateaus identified on the charge and discharge curves (Figure 2f). The newly developed cathode yielded an exceptional average discharge voltage of 4.2 V together with an energy density of 970 Wh kg^{-1}, which was twice as high as that of transition-metal intercalation cathodes (*e.g.*, $LiMn_2O_4$ and $LiCoO_2$). In addition, under 0.2 C, the graphite‖$(LiBr)_{0.5}$-$(LiCl)_{0.5}$–graphite full cell delivered a dependable discharge capacity of 127 mAh g^{-1} (based on the total electrode active material mass) with an average voltage of 4.1 V. After 150 cycles, it maintained 74% of its initial capacity with an average CE of 99.8%.

Despite the aforementioned merits, utilizing WISE electrolytes raises concerns in terms of high salt cost, poor water wettability, and environmental hazards. To address these issues, Suo *et al.* [31] investigated the impact of dissolved gases on the reduction of WISE components. They found that CO_2 has a strong selective affinity to WISE, as indicated by the chemical shift of ^{19}F NMR spectra (Figure 3a). By adding CO_2 as an interphase-forming additive in aqueous electrolytes, the aqueous batteries were able to achieve a wide electrochemical window comparable to that of WISE with only 5 mol L^{-1} LiTFSI, therefore reducing the expensive excess use of Li salt. The diluted electrolyte with the introduction of CO_2 delivered an initial capacity of 90 mAh g^{-1}, along with a retention rate of 88% after 50 cycles (Figure 3b). In contrast, the WISE showed a low capacity of only 25 mAh g^{-1}. Furthermore, an electrolyte consisting of a diluted 2 mol L^{-1} LiTFSI solution in 94% polyethylene glycol (PEG) and 6% water was developed by Lu *et al.* [32], in which water molecules were mainly hydrogen-bonded to the PEG performing as a crowding agent. This electrolyte did not exhibit a significant amount of free water molecules, leading to a lowered HER potential and an electrochemical stability window of 3.2 V. The reversibility of the $Li_{1.3}Al_{0.3}$-$Ti_{1.7}PO_4$-coated $Li_4Ti_5O_{12}$ anode (L-LTO) and $LiCoO_2$ cathode in such electrolyte was confirmed by the cyclic voltammetry (CV) measurements (Figure 3c). The corresponding full cell displayed a high average CE of 99% after 300 cycles at 1 C, with the minimal electrolyte decomposition. Apart from this, Wang *et al.* [33] introduced a localized water-in-salt (LWIS) electrolyte comprising low-cost lithium nitrate ($LiNO_3$) salt and an inert diluent, 1,5-pentanediol (PD). The incorporation of PD preserved the solvation structure of the WISE, enhancing the electrolyte
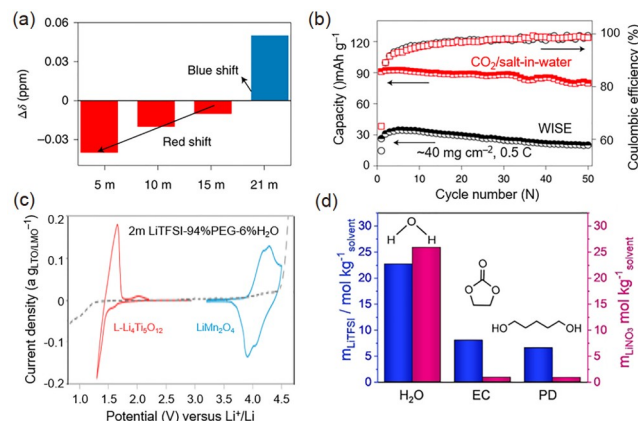

Figure 3 Aqueous electrolyte systems beyond WISE for high-energy LIBs. (a) Chemical shifts of ^{19}F NMR spectra for the LiTFSI electrolyte with different concentrations [31]. (b) Cycling performance of the CO_2/salt-in-water and water-in-salt electrolyte (WISE)-based cell under a thick electrode (40 mg cm^{-2}, 334 μm) at 0.5 C [31]. (c) CV profiles collected in 2 mol L^{-1} LiTFSI–94%PEG–6%H_2O electrolyte at 0.2 mV s^{-1} for $LiMn_2O_4$ and $Li_4Ti_5O_{12}$ [32]. (d) Solubilities of LiTFSI (blue) and $LiNO_3$ (pink) in different solvents at 25 °C [32] (color online).

stability through the interactions with water and NO_3^- ions, and reducing the overall concentration of salts. Especially, compared with the organic LiTFSI salt, the high solubility of inorganic $LiNO_3$ salt in water (up to 25 mol L^{-1}) and its limited solubility in diluents make it a suitable choice for the development of LWIS electrolytes (Figure 3d). The stability window of the LWIS electrolyte can be expanded to 3.0 V by the *in-situ* gelation with the tetraethylene glycol diacrylate (TEGDA) monomer. The Mo_6S_8|LWIS gel electrolyte| $LiMn_2O_4$ batteries exhibited exceptional cycling performance, with a CE of 98.53% after 250 cycles at 1 C. Above studies provide new insights for the development of high-energy aqueous LIBs.

2.2 Aqueous Na-ion and K-ion batteries

In comparison to their Li equivalents, aqueous SIBs and PIBs seem to be a much more economically feasible option, given the plentiful availability of their reserves on earth. However, the larger ionic radius of Na^+ (0.102 nm) and K^+ (0.138 nm) presents a challenge for the development of electrode materials for aqueous Na-/K-ion batteries. The promising results of WISE used in aqueous LIBs offer a new possibility to expand the electrochemical stability windows of aqueous electrolytes for aqueous SIBs and PIBs. Na-based WISE was successfully constructed when the concentration of sodium triflate (NaOTF) was increased to 9.26 mol L^{-1} in water [34]. According to CV curves, the electrochemical stability window of this WISE was expanded to ~2.5 V, and widened enough to encompass the electrochemical couple of $Na_{0.66}[Mn_{0.66}Ti_{0.34}]O_2$ and $NaTi_2(PO_4)_3$ (Figure 4a). Consequently, the corresponding full cell achieved exceptional CE
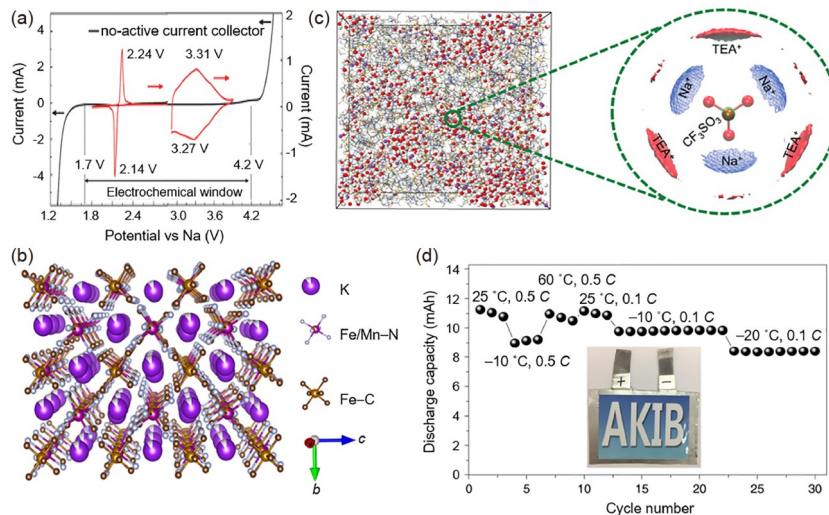
Figure 4 Aqueous SIBs and PIBs. (a) CV curves measured on inert electrodes at the scanning rate of 10 mV s^{-1}, which was overlaid with the 1st CV traces obtained on the active anode (NaTi$_2$(PO$_4$)$_3$) and cathode (Na$_{0.66}$[Mn$_{0.66}$Ti$_{0.34}$]O$_2$) materials at the scanning rate of 0.1 mV s^{-1} [34]. (b) A snapshot of the molecular dynamics (MD) simulation box for the IC-WiS electrolyte with water and Na$^+$ highlighted and TEAOTF shown as the wireframe. The right section is an isosurface showing most probable positions (8.5 times the average) of the TEA$^+$ nitrogen atom (red mesh) and Na$^+$ (blue mesh) around the CF$_3$SO$_3^-$ anion [35]. (c) Typical structure of the K$_x$Fe$_y$Mn$_{1-y}$[Fe(CN)$_6$]$_w$·zH$_2$O in the $P2_1/n$ space group [36]. (d) Cycling performance of the PTCDI|22 mol L^{-1} KCF$_3$SO$_3$|K$_x$Fe$_y$Mn$_{1-y}$[Fe(CN)$_6$]$_w$·zH$_2$O pouch cell at different rates (0.5/0.1 C) and temperatures (−20/−10/25/60 °C) from 0 V to 2.3 V [36] (color online).

(>99.2%) at a low rate (0.2 C) for >350 cycles, as well as outstanding cycling stability with the minimal capacity loss (0.006% per cycle) at a high rate (1 C) for >1,200 cycles. However, different from aqueous LIBs, the available formation of Na-based WISE is significantly hindered by the lower solubility of Na salts than that of Li salts. On the other hand, applying a mixed-cation bi-salt strategy may result in adverse effects, such as the co-intercalation of the secondary cation species.

To tackle the aforementioned concerns, a novel type of electrolyts called inert-cation-assisted water-in-salt (IC-WiS) was proposed [35]. Such electrolytes utilized 9 mol L^{-1} NaOTF and 22 mol L^{-1} tetraethylammonium triflate (TEAOTF) as salts with TEA$^+$ as the inert-cation and therefore delivered an exceptionally high total concentration of 31 mol L^{-1}. The large radius of TEA$^+$ blocked its insertion into a majority of electrode materials, thus ensuring an expanded electrochemical stability window up to 3.3 V. Notably, the viscosity was significantly lower than that of Li-based bi-salt electrolytes, as verified by molecular dynamics (Figure 4b). The distinctive advantages of this electrolyte enabled the coupling of the NaTiOPO$_4$ anode and Prussian blue analog of Na$_{1.88}$Mn[Fe(CN)$_6$]$_{0.97}$·1.35H$_2$O cathode in full cells, which exhibited an average voltage of 1.74 V, high energy density of 71 Wh kg^{-1}, and remarkable capacity retention of 90% after 200 cycles at 0.25 C and 76% over 800 cycles at 1 C.

The choice of electrode materials and electrolytes in aqueous PIBs is strongly limited by the considerably larger ionic radius and higher ionization potential of K$^+$. Breakthrough came when Hu *et al*. [36] constructed a system using

K$_x$Fe$_y$Mn$_{1-y}$[Fe(CN)]$_w$·zH$_2$O as the cathode (Figure 4c), 3,4,9,10-perylenetetracarboxylic di-imide (PTCDI) as the anode and highly concentrated 22 mol L^{-1} KCF$_3$SO$_3$ aqueous solution as the electrolyte, marking the realization of full aqueous PIBs. Particularly, the specific water-in-salt solvation structure of K$^+$ benefited to minimize the dissolution of both electrodes, while the Fe-substituted cathode demonstrated the excellent cycling performance due to the prevention of the formation of the tetragonal phase. Consequently, the as-proposed full battery delivered a high energy density of 80 Wh kg^1 and 73% capacity retention after 2,000 cycles at 4 C, together with excellent wide-temperature-range cyclability (Figure 4d). The development of aqueous SIBs and PIBs relies on the further exploration of new electrode couples and compatible aqueous electrolytes.

3 Aqueous Zn-ion batteries

Rechargeable aqueous ZIBs are considered as promising AMBs for the grid-scale energy storage, because of their high theoretical specific capacity based on two-electron redox chemistry, and several merits of inexpensiveness, natural abundance, nontoxicity, low redox potential (−0.76 V *vs*. SHE), high overpotential in water for the hydrogen evolution, easy to processing, and environmental benignity. Furthermore, the employment of high ion conductivity (>40 mS cm^{-1}) and non-flammable aqueous electrolytes propels such a ZIB system to be feasible for the stationary grid-scale application when taking cost, safety, and lifetime into consideration. In addition, when a neutral electrolyte is in-

troduced, the Zn passivation problem that existed in the conventional alkaline Zn−MnO₂ battery can be much improved [37–39].

The ZIBs are mainly composed of three parts: cathode, zinc anode and aqueous electrolyte. The Zn foil/powder/alloy exhibits relatively good stability and accepted resistance to corrosion in water/air. Zn ions repeatedly dissolve and deposit on the Zn anode during the charging and discharging. Mild and slightly acidic Zn salt solutions (pH=3.6–6.0) configured by dissolving Zn salts in water (*e.g.*, $ZnSO_4$, Zn $(CF_3SO_3)_2$, $ZnCl_2$, $Zn(NO_3)_2$, and $Zn(CH_3COO)_2$) are preferentially employed as electrolytes. The Zn anode suffers from the surface oxidation owing to the high oxidability of NO_3^-, leading to a fast performance degradation in $Zn(NO_3)_2$-based electrolytes [40]. The $ZnCl_2$-based electrolyte displayed a narrow potential window. For the $Zn(CH_3COO)_2$-based electrolyte, the incomplete ionization results in a low ionic conductivity. In the $Zn(CF_3SO_3)_2$-based electrolyte, $CF_3SO_3^-$ efficiently reduces the number of water molecules around Zn^{2+} ions. This solvation effect efficiently prevents the progression of HER and avoids the formation of Zn dendrites [41–43]. A wide variety of materials, such as manganese (Mn)-based, vanadium (V)-based, metal organic framework (MOF)/covalent organic framework (COF) compounds, organics, Mo-based materials and ever porous conductors, are suitable for the use as the cathodes of ZIBs.

3.1 Mechanism and cathode chemistry

3.1.1 Manganese-based cathode materials

MnO_2 is a widely investigated polymorphic inorganic material in ZIBs, which are mainly categorized into two microscopic forms: layered MnO_2 and tunnel MnO_2 (Figure 5a). The layered polymorphs (δ-MnO_2) are constructed by only edge-sharing [MnO_6] octahedra across the basal plane, while the tunnel polymorphs (α-MnO_2 (4.6 Å×4.6 Å), β-MnO_2 (2.3 Å×2.3 Å), γ-MnO_2 (2.3 Å×4.6 Å and 2.3 Å ×2.3 Å), R-MnO_2 (2.3 Å×4.6 Å) and t-MnO_2 (6.9 Å×6.9 Å)) contain both edge-sharing and corner-sharing [MnO_6] units. The angstrom-level opening frameworks generally accommodate various cations that support the large openings and enrich MnO_2's (electro)chemical activity toward various reactions [44]. In 2012, Kang *et al.* [22] elaborated the concept of neutral ZIBs, during which α-MnO_2 was adopted as a cathode coupled with the Zn foil anode in the $ZnSO_4$ or $Zn(NO_3)_2$ aqueous electrolyte. As demonstrated in Figure 5b, two distinguishable peaks appeared at around 1.3 V and 1.7 V *vs*. Zn/Zn^{2+} during the cycling, corresponding to the storage/release of Zn^{2+} ion insertion/extraction of crystalline α-MnO_2. Meanwhile, the assembled Zn|MnO_2 full cell exhibited excellent electrochemical stability. A high capacity retention rate of 100% was achieved after 100 cycles at 6 C, and the CE was almost 100%.
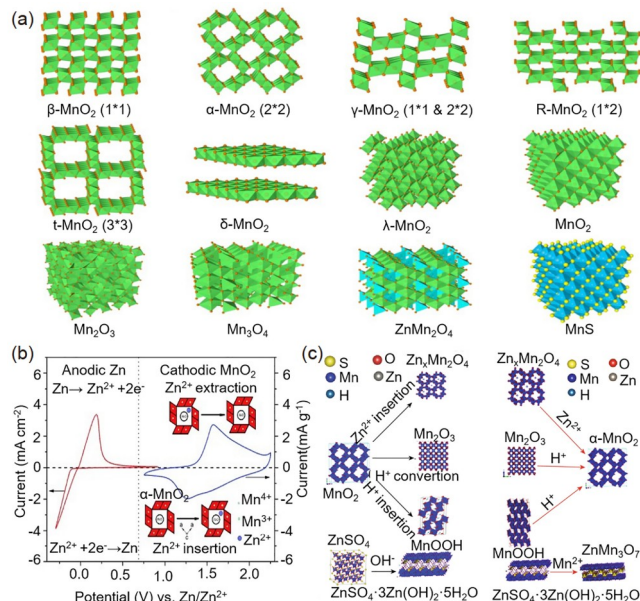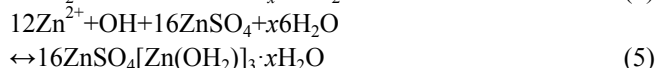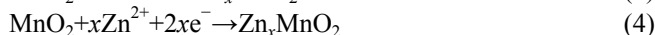

Figure 5 Crystal structure and reaction mechanism of Mn-based cathode materials for ZIBs. (a) Crystal structure of Mn-based compounds [44]. (b) Cyclic voltammogram of the zinc anode (red line) and α-MnO_2 cathode (blue line) at 2 mV s^{-1} [22]. (c) Phase evolution of the cathode during the first discharge (left) and charge process (right) [46] (color online).

Based on the existing storage mechanisms, accompanied by generating complex products, undergoing severe phase transitions as well as slow reaction kinetics in the process of the ion storage, it is difficult to realize the potential of Mn-based materials. It should be mentioned that the high capacity and long-term cycling of ZIBs may be obtained involving multi-mechanisms through optimized cathode materials. The generally recognized energy storage mechanisms of MnO_2 for ZIBs are summarized as follows (Figure 5c) [45–47]:

$$H_2O \leftrightarrow H^+ + OH^- \tag{1}$$
$$MnO_2 + H^+ + e^- \leftrightarrow MnOOH \tag{2}$$
$$MnO_2 + xH^+ + xe^- \leftrightarrow H_xMnO_2 \tag{3}$$
$$MnO_2 + xZn^{2+} + 2xe^- \rightarrow Zn_xMnO_2 \tag{4}$$
$$12Zn^{2+} + OH + 16ZnSO_4 + x6H_2O$$
$$\leftrightarrow 16ZnSO_4[Zn(OH_2)]_3 \cdot xH_2O \tag{5}$$

The cathode reaction may involve the H^+/Zn^{2+} (de)intercalation/conversion (equation (2–4)), shifting equilibrium of water reaction (equation (1)), and the formation of $ZnSO_4[Zn(OH_2)]_3 \cdot xH_2O$ species due the change of pH value on the cathode/electrolyte interfaces (equation (5)). The reversibly formed/decomposed $Zn_4(OH)_6SO_4 \cdot xH_2O$ on the surface of MnO_2 during the discharge/charge seemly supported the H^+ (de)intercalation mechanism [48]; however, the consumption of H^+ in an electrolyte by the proton-coupled deposition mechanism may also lead to the partial elevation of pH on cathode|electrolyte interfaces. Furthermore, the absence of Zn^{2+} in discharged MnO_2 by the direct atomic imaging in reference may also challenge the Zn^{2+} (de)intercalation me-

chanism [49].

In the H^+/Zn^{2+} (de)intercalation-dominated battery systems, Mn^{2+} was considered to suppress, inhibit, or discourage the manganese dissolution caused by the Jahn–Teller effect, with the underlying assumption that it changes the equilibrium of Mn dissolution from the MnO_2 electrode [50]. The $MnSO_4$ additive has been commonly applied in almost every ZIB system. However, this reasoning is hard to be followed, given that the preadded concentration of Mn^{2+} remains low (0.1–0.3 mol L^{-1}) and thus far from saturation [51].

According to the Nernst equation, the proton concentration is closely related to the Mn deposition potential. A decrease in the H^+ ion content reduces the energy requirement for the Mn deposition, while the formation of oxidized manganese is more easily triggered at relatively higher pH values. In electrolytes with mild pH values, the deposition/dissolution of Mn^{2+} (typically involving single electron transfer) will mix with the deintercalation/intercalation of Zn^{2+} (H^+/Zn^{2+} dominant region); the main contribution to the capacity is the ion deintercalation due to the high deposition potential of Mn. The corresponding capacity evolution curve is relatively stable, which can be attributed to the fixed number of ion storage sites in the electrode material. With the progression of cycling, pH and capacity increase continuously, and the dominant process shifts to Mn^{2+} deposition. As the pH value further increases, capacity decays and a large amount of inert "dead Mn" is formed, resulting in the sharp capacity attenuation [15,47].

For instance, Weng and Yang *et al.* [47] revealed that the deposition/dissolution process was a pH-dependent Mn(III)-intermediates (MnOOH and Mn^{3+}) by an *in-situ* electrochemical quartz crystal microbalance technique. During the deposition process, MnOOH is the Mn(III)-intermediate in neutral electrolytes. As the proton concentration increases, Mn^{3+} gradually becomes the main Mn(III)-intermediate, but the deposition kinetics of MnO_2 become sluggish, and thus more residual Mn^{3+} cannot be further oxidized to MnO_2. Sufficient proton concentration (pH=4) is necessary for the dissolution reaction of MnO_2 [47]. However, in acidic electrolytes, MnO_2 is first reduced to MnOOH rather than Mn^{3+}. More MnOOH is chemically dissolved in Mn^{3+} but cannot be totally reduced to Mn^{2+} with increasing the proton concentration [48]. The dissolution of MnOOH and disproportionation of Mn^{3+} can induce the generation of residual MnO_2 on the cathodes and "dead" MnO_2 outside the cathodes, which become the inert species [52]. In addition, excessive proton concentration will lead to an increased pH due to the existence of plentiful OH^- in a local scope, which promotes the formation of $Zn_4SO_4 \cdot (OH)_6 \cdot xH_2O$ as harmful by-products [42].

In addition to the proton co-intercalation, the MnO_2 cathode also undergoes complex side reactions, including $MnO_2/$

Mn^{2+} dissolution–deposition. The Mn^{2+} and H^+ ions involved in manganese dissolution–deposition mechanisms have attracted attention due to some unfamiliar phenomena, such as a higher specific capacity than the theoretical value of the single-electron transfer, the reversible fluctuation of pH values and Mn^{2+} concentration of electrolyte, and the reversible formation and disappearance of porous Mn matrix at the electrode interface, which directly affects the electrochemical performance [53].

Manganese oxide materials generally suffers from dissolving issues due to the Jahn–Teller effect, which describes the configuration distortions for the electronic cloud of a nonlinear molecule with multiple degenerate states [1]. In the case of octahedral MnO_6 with a nonlinear magnetic field, Mn^{3+} exhibits a high spin state with a very large magnetic moment, and MnO_2 typically undergoes collinear Jahn–Teller distortions along the elongated axis. For octahedrally coordinated high spin Mn^{3+} or Mn^{4+} cations, only one electron occupies the e_g orbital, leading to an asymmetric occupation. The electrons distributed in orbitals such as $d_{x^2-y^2}$ and d_{z^2} possess different shielding effects for Mn atomic nuclei with different orientations. In this configuration, the entire d orbital no longer conforms to the octahedral O_h symmetry, rendering the central Mn^{3+} cation unstable. To stabilize Mn^{3+} cations, the two longitudinal Mn–O bonds in the octahedral MnO_6 are elongated while the other four equatorial Mn–O bonds undergo the compression. This distortion causes the MnO_6 octahedron to deviate from the O_h symmetry to D_{4h}, weakening the system's symmetry and lowering the energy by eliminating degenerate orbitals and undergoing structural distortion [54,55].

To strengthen the stability and alleviate the dissolution of Mn-based cathode materials, defect engineering was adopted, which can reduce the overall formation energy of manganese oxides and enhance the charge transfer and reaction kinetics [56]. For example, the incorporation of K^+ ions can intrinsically stabilize the Mn-based cathode *via* forming oxygen defects to improve the electrical conductivity of $K_{0.8}Mn_8O_{16}$, and open the MnO_6 polyhedron walls for the ion diffusion. Therefore, a significant energy output of 398 Wh kg^{-1} (based on the mass of the cathode) and durability over 1,000 cycles with no obvious capacity fading are obtained [57]. Anionic doping, such as S-doped MnO_2 (S-MnO_2), was also employed to substitute the high electronegative oxygen in MnO_2 to ameliorate the electronic structure of MnO_2 by lowing its bandgap and improving the intrinsic electronic conductivity to weaken the electrostatic interaction between Zn^{2+} ions and the cathode structure [58]. As a result, the S-MnO_2 cathode delivered a maximum specific capacity of 324 mAh g^{-1} at a current density of 200 mA g^{-1} and a stable reversible capacity of 150 mAh g^{-1} with the capacity retention of 95% over 1,000 cycles at a current density of 3,000 mA g^{-1} [48].

Morphological control of Mn-based electrode materials is another effective way to improve the electrochemical activity and kinetics. Nanofibre-, nanorod-, nanoribbon- and nanobelt-like MnO_2 can be easily prepared *via* hydrothermal methods. The transformation of micrometre-long nanofibres to a well-mixed composite of short nanorod aggregations after the initial cycle can stabilize and enhance the structural mechanics and kinetics of the electrodes by releasing the strain and reducing the diffusion length for ions and electrons in the nanocomposite structure, resulting in the excellent rate and cycling stability of the $Zn|MnO_2$ aqueous batteries [50].

Generally, Mn-based materials have another common barrier, inherently poor electrical conductivity. To solve this problem, researchers combine them with highly conductive additives to form Mn-based material/conductive additive composites, such as MnO_2/graphene [59,60], MnO_2/carbon nanotube [61,62], and MnO_2/carbon [37,51,63]. Carbon nanomaterials with large exposed specific surface area enable them to serve as nano/microscale conductive substrates for cathode materials, facilitating the fast electron transfer and acting as matrixes to embed active materials. However, fully embedding into the carbon matrixes with inferior ion transfer will decrease the utilization of active materials [64]. Furthermore, the direct contact between cathode materials and aqueous electrolytes can be effectively avoided, relieving the attenuation of cathode materials. In general, pristine carbon materials are required to be functionalized and/or doped with heteroatoms (*e.g.*, N, P, S, B), for improving the intrinsic low wettability and poor reactivity for better applicability. Li *et al.* [37] reported a free-standing cathode with hierarchical core–shell MnO_2@nanowires (MnO_2@NC) by incorporating layered MnO_2 with N-doped carbon nanowires. The N atom elongated the Mn–O bond and reduced the valence of the Mn^{4+} ion in the MnO_2 crystal by delocalizing its electron clouds. Thus, the electrostatic repulsion was weakened when Zn^{2+}/H^+ was inserted into the host MnO_2 lattices, which was profitable to more cation insertion and faster ion transfer kinetics for the higher capacity and rate capability. The obtained MnO_2@NC electrode showed an enhanced specific capacity (325 mAh g^{-1} at 0.1 A g^{-1}) and rate performance (90 mAh g^{-1} at 2 A g^{-1}), as well as improved cycling stability.

In addition to MnO_2, other manganese-based oxides, *e.g.*, Mn_2O_3 and Mn_3O_4, have also been investigated for the reversible Zn-ion storage [56,65,66]. Mn_2O_3 with a bixbyite structure was first used as the cathode of ZIBs by Kang's group in 2017. During the insertion of Zn^{2+}, the bixbyite transforms into layered Zn-birnessite and Mn^{3+} undergoes a reduction reaction to form Mn^{2+} simultaneously [66]. Recent study also confirms the co-insertion/extraction of H^+ and Zn^{2+} in the Ni-doped Mn_2O_3 cathode [56]. Mn_3O_4 with the spinel structure has also been used as the cathode of ZIBs. Related study shows that initial Mn_3O_4 is converted to

ramsdellite MnO_2 for the insertion and extraction of H^+ and Zn^{2+} [65].

3.1.2　Vanadium-based cathode materials

The layered $Zn_{0.25}V_2O_5 \cdot nH_2O$ was first reported as the Zn^{2+} hosting material for ZIBs in 2016, as shown in Figure 6a [67]. Since then, V-containing materials have been intensively studied because the wide redox range of vanadium ($V^{5+} \leftrightarrow V^{4+} \leftrightarrow V^{3+}$) increases its chances to fit in the limited potential window of water. Vanadium oxides (such as VO_2, V_2O_3, V_2O_5 ($V_2O_5 \cdot nH_2O$), $V_3O_7 \cdot H_2O$ ($H_2V_3O_8$), $V_5O_{12} \cdot H_2O$, V_6O_{13} ($V_6O_{13} \cdot nH_2O$), and $V_{10}O_{24} \cdot 12H_2O$), especially the layered vanadium oxides, are particularly attractive due to their high specific capacity (usually >300 mAh g^{-1}), natural abundance, and favorable processability owing to the large interlayer distances facilitating the Zn^{2+} (de)intercalation [68]. Different from crystalline structures, amorphous VO_x materials with the short-range ordering V–O polyhedral present the random network arrangement, which may provide more active sites for the ion insertion, reduce the ion diffusion length, and accommodate the lattice strain during the repeated charge/discharge processes [69].

The energy storage mechanism of vanadium-based cathode materials based on the insertion of Zn ions associated with the proton co-intercalation has been widely proven. The H^+ insertion dominated the high-voltage and high-rate electrochemical process while the insertion of Zn^{2+} controlled the low-voltage state and low-rate electrochemical process [70]. In general, V-based materials are slightly soluble in water, exhibiting a characteristic pale-yellow color. Such poor structural stability of vanadium-based materials in aqueous electrolytes leads to the chemical dissolution and formation of soluble V-based substances, giving rise to rapidly decreased capacity [71]. For commonly used aqueous solutions in ZIBs (pH~4), its dissolution follows the equation: $V_2O_5 + 3H_2O \rightarrow 2VO_2(OH)_2^- + 2H^+$. Further, the soluble $VO_2(OH)_2^-$ can react with Zn^{2+} in the electrolyte, forming $Zn_3V_2O_7$-$(OH)_2 \cdot 2H_2O$ compound ($2VO_2(OH)_2^- + 3Zn^{2+} + 3H_2O \rightarrow Zn_3V_2O_7(OH)_2 \cdot 2H_2O + 4H^+$). Therefore, maintaining the structural stability of vanadium-based cathodes against the dissolution in aqueous electrolytes is crucial for extending the ZIB lifespan. [72].

Introducing defects such as cationic or anionic vacancies in the crystal lattices is beneficial to suppress the needless phase transition and provide more activated sites for enhanced Zn ion storage capacity [73,74]. It has been demonstrated that oxygen vacancies ($VO^{\bullet\bullet}$) can increase the interlayer spacings of metal oxides and improve their ion diffusion kinetics, favoring the fast ion insertion and extraction. Li *et al.* [75] reported that $VO^{\bullet\bullet}$-rich VO_2 (B) achieved a specific capacity of 375 mAh g^{-1} at a current density of 100 mA g^{-1} and long-term cyclic stability with the retained specific capacity of 175 mAh g^{-1} at 5 A g^{-1} over
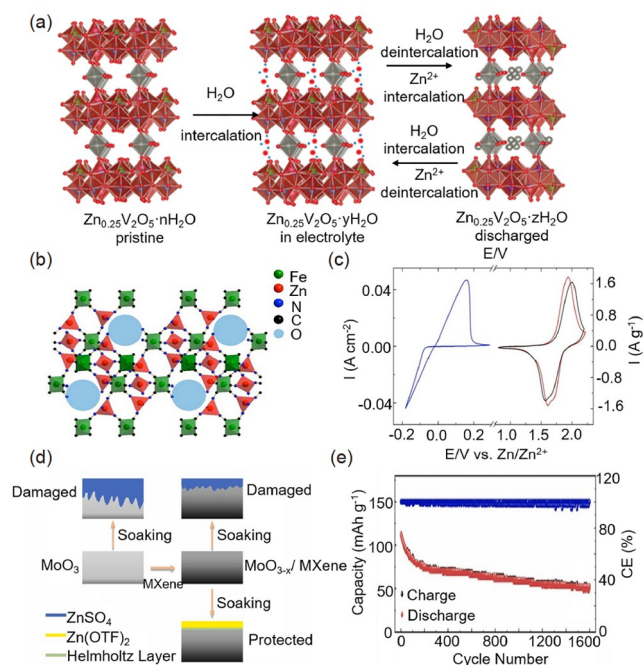
Figure 6 Zn storage mechanism and electrochemical properties of representative cathode materials. (a) Scheme showing reversible water intercalation into $Zn_{0.25}V_2O_5 \cdot nH_2O$, and the water deintercalation accompanying Zn^{2+} intercalation upon electrochemical discharge [67]. (b) Crystal structure of rhombohedral zin hexacyanoferrate [89]. (c) Typical CV curves of two individual electrodes (Zn anode and ZnHCF cathode) along with the full cell at a scan rate of 2 mV s^{-1} [89]. (d) The protection mechanism of the MoO_{3-x}/MXene cathode. $Zn(OTF)_2$ [110]: zinc trifluoromethanesulfonate. (e) Cycle life of the optimal MoO_{3-x}/MXene papers [110] (color online).

2,000 cycles (85% capacity retention), higher than that of VO_2 (B) nanobelts (280 mAh g^{-1} at 100 mA g^{-1} and 120 mAh g^{-1} at 5 A g^{-1}, 65% capacity retention). Zheng *et al.* [76] presented that the partial removal of ammonium cations introduced oxygen vacancies in $NH_4V_4O_{10}$, which not only weakened the strong electrostatic interaction between the V–O layer and Zn^{2+} to reduce the energy barrier of the Zn^{2+} diffusion process, but also decreased the R_{ct} to accelerate the reaction kinetics. As a consequence, the specific capacity of the oxygen vacancy-rich $NH_4V_4O_{10}$ was enhanced from 304 mAh g^{-1} to 355 mAh g^{-1}, relative to the sample without treatment.

Doping is another effective method to modulate the structure of V-based cathodes. Various guest species such as cations (Li^+, K^+, NH_4^{4+}, Mg^{2+}, Ca^{2+}, Ba^{2+}, La^{3+}, *etc*.) [77–79] and polymers (polyaniline, C_3N_4, *etc*.) [80–82] were introduced between the layers of layered-vanadium oxides to sustain the framework by the introduction of oxygen defects, improved conductivity, and minimized electronic interactions between Zn^{2+} ions and host materials during the discharge process. For example, K^+-doped ammonium vanadate was reported recently that K^+ replacing NH_4^{4+} alleviated the irreversible de-ammoniation to prevent the structural col-

lapse during the ion insertion/extraction because the electron structure was modulated and Zn-ion diffusion path with a lower migration barrier was obtained. Thus, potassium ammonium vanadate exhibited a high discharge capacity (464 mAh g^{-1} at 0.1 A g^{-1}) and excellent cycling stability (90% retention over 3,000 cycles at 5 A g^{-1}) [83].

The incorporation of conductive carbonaceous components as the surface coating or support has been widely adopted to address the structural degradation of layered V-based cathodes [84]. The conductive carbon materials, such as reduced graphene oxide (rGO) can effectively improve the electron transfer in the cathode [85]. Niu *et al.* [86] synthesized an amorphous V_2O_5/carbon composite material (*a*-V_2O_5@C) through the derivatization of a MOF as a cathode material for ZIBs. The capacity of *a*-V_2O_5@C can be maintained at 249.2 mAh g^{-1} after 20,000 cycles at a high current density of 40 A g^{-1}. Chen *et al.* [87] reported that single-crystal V_2O_5 samples well-encapsulated by the amorphous carbon showed outstanding electrochemical performance because of the improved conductivity and dramatically decreased energy loss by the thin amorphous carbon layer.

3.1.3   MOF/COF and organic cathode materials

Conductive MOFs and COFs constructed by coordinating metal ions and π-conjugated organic ligands have been employed in ZIBs with the high thermal and chemical stability owing to the nature of their architectures in which small molecular units are linked *via* covalent bonds [88]. Prussian blue and its analogues (PBAs) possess a general formula of $A_xM_1[M_2(CN)_6]_y \cdot nH_2O$ with the face-centered cubic structure. The open-framework structure has large channels and allows the rapid diffusion of Zn ions, giving PBAs an excellent cycle life and high-rate capability as cathode materials in aqueous electrolytes. For example, rhombohedral zinc hexacyanoferrates (ZnHCFs) exhibit a porous 3D framework with FeC_6 octahedra linking to ZnN_4 tetrahedra *via* CN ligands. Alkaline cations A (A = Na^+, K^+ and Cs^+) and water molecules are located in the large open sites which can behave as the intercalation hosts for various cations. When combined with a zinc anode, zinc hexacyanoferrate was reported to yield an average operation voltage of ~1.7 V and delivered a specific energy density of 100 Wh kg^{-1} based on the total mass of the active electrode materials, which was demonstrated in Figure 6b and c [89]. Kang's group [90] reported a high-performance aqueous ZIB using the manganese trimesic acid (Mn(BTC)) cathodes and the ZIF-8@Zn anodes, which exhibited a capacity of 112 mAh g^{-1} and excellent cycling stability with 92% capacity retention after 900 charge/discharge cycles.

Properly stacked low-dimensional (0D/1D/2D) MOFs with well-defined pore channels and stable skeletons are ideal materials for the Zn^{2+} transport [91]. Banerjee *et al.*

[92] reported the use of a classical 2D COF HqTp as the cathode material for rechargeable aqueous ZIBs, delivering a specific capacity of 276.0 mAh g^{-1}. Stoddart *et al*. [93] reported a conductive 2D Cu$_3$(HHTP)$_2$ cathode delivering a capacity of 228 mAh g^{-1} at 50 mA g^{-1}. The high diffusion rate of Zn^{2+} ions and low interfacial resistance by the insertion of hydrated Zn^{2+} ions allowed Cu$_3$(HHTP)$_2$ to follow the intercalation pseudocapacitance mechanism. As a consequence, Cu$_3$(HHTP)$_2$ achieved a high rate performance and cyclability, indicating that 75.0% of the initial capacity (124.4 mAh g^{-1}) was maintained after 500 cycles at a high current density of 4,000 mA g^{-1} (~18 C). Ciesielski *et al*. [94] synthesized a new olefin-linked benzothiadiazole-based 2D-COF, in which benzothiadiazole units were explored as novel electrochemically-active groups, delivering a capacity of 283.5 mAh g^{-1}. Both nitrogen and sulfur atoms were highly suitable for hosting, through reversible non-covalent interactions, monovalent and bivalent cations, offering additional control over the process of ion complexation and release.

The intrinsically low electrical conductivity of most MOFs severely limits the effective utilization of built-in redox centers, resulting in a low capacity and power density. For this reason, constructing heterostructures based on 2D MOFs as the host and other conductive 2D materials (graphene, CNT, carbon fibers, carbon black, *etc*.) as guests can induce a more effective mass/charge transport [95]. Wong *et al*. [96] reported an alternately stacked MOF/MXene heterostructure, exhibiting a 2D sandwich-like structure with abundant active sites, improved electrical conductivity and exceptional structural stability. Based on a reversible intercalation mechanism of zinc ions and high electrical conductivity in the 2D heterostructure, the as-developed cathode material showed a rate performance of 260.1 mAh g^{-1} at 0.1 A g^{-1} and 173.1 mAh g^{-1} at 4 A g^{-1}, and 92.5% capacity retention over 1,000 cycles at 4 A g^{-1}.

Organic electrode materials are only composed of sustainable elements (such as C, H, O, N and S) and their structures can be designed flexibly. Furthermore, the redox chemistry in organic electrode materials of ZIBs is only accompanied by the rearrangement of chemical bonds instead of the insertion/extraction of large hydrated Zn^{2+}, avoiding large structural changes that generally exist in inorganic compounds [97–100]. Therefore, organic materials are considered as promising cathode materials of aqueous ZIBs. Organic materials store charges *via* n-type or p-type reactions [101]. The n-type organic materials with redox functional groups are capable of reversible Zn^{2+} storage by the coordination reactions between Zn^{2+} ions and active sites, such as carbonyl and imine compounds (*e.g.*, quinone compounds [102,103], pyrene-4,5,9,10-tetraone (PTO) [104], diquinoxalino [2,3-*a*:2′,3′-*c*] phenazine (HATN) [105], and hexaazatrinnphthalene-2,8,14-tricarbonitrile (HATN-3CN)) [106], avoiding the structural collapse that prevails among

inorganic cathodes. The excellent redox activity of quinones also makes them desirable cathode materials for aqueous ZIBs, achieving a capacity of 335–225 mAh g^{-1} at 20–30 mA g^{-1} mainly through the co-insertion of Zn^{2+} and water. Despite the as-mentioned advantages, organic cathodes still suffer some intractable issues including insufficient conductivity which lowers the utilization of active redox sites, hindering the release of charge-storage capacities; and the easy dissolution of organic molecules or discharged products in aqueous electrolytes, which chronically decays the lifespan of ZIBs [106,107].

3.1.4   Other cathode materials

Zhang *et al*. [108] reported a porous VSe$_{2-x}$·nH$_2$O host for Zn^{2+} storage. The co-modulation of H$_2$O intercalation and selenium vacancies enables to enhance the interfacial Zn ion capture ability and decreasing the Zn ion diffusion barrier. As a result, the cathode retained a high specific capacity of 173 mAh g^{-1} after 5,000 cycles at 10 A g^{-1}, as well as a high energy density of 290 Wh kg^{-1} and a power density of 15.8 kW kg^{-1} at room temperature. Kang's group [109] reported that MnS delivered a cycling discharge capacity of 110 mAh g^{-1} at a current density of 500 mA g^{-1}, and maintained a reversible discharge capacity of 70 mAh g^{-1} after 100 cycles, which was approximately 63.6% of the value of the first discharge capacity.

MoO$_3$ is considered as a promising cathode material for the energy storage with huge potential windows due to its higher theoretical capacity and excellent electrochemical activity. However, the low conductivity and poor stability of MoO$_3$ in aqueous electrolytes seriously affect its wide application. To solve the problems, Gao *et al*. [110] investigated Ti$_3$C$_2$T$_x$ (MXene) with a two-dimensional (2D) layered structure and hydrophobic trifluoromethane sulfonate (OTf$^-$) for the ZIBs, as shown in Figure 6d and e. The MXenes not only caused the partial reduction of MoO$_3$ to form oxygen vacancies, but also reduced the hydrophilicity of MoO$_3$. The OTf$^-$ in the zinc trifluoromethane sulfonate (Zn(OTf)$_2$) electrolyte was conducive to preventing the cathode from dissolving. As expected, MoO$_{3-x}$/MXene delivered a capacity of 369.8 mAh g^{-1} at 0.20 A g^{-1} and a cycling life of 46.7% capacity retention after 1,600 cycles.

It is well known that the pH value is closely related to the proton-coupled reactions and electrochemical behaviors of the cathode. From the perspective of reaction equilibrium, a mild pH value is beneficial for the deposition of the cathode carriers, while an excess of hydroxide ions suppresses the dissolution of cathode. As a result, an increase in pH value reduces the contribution of the deposition/dissolution capability and shifts the electrochemical mechanism to the ion insertion region [111,112]. Therefore, controlling the pH environment and related proton-coupled reactions is crucial for achieving the desired performance.

3.2   Strategies for stabilizing Zn anodes

The Zn dendrite formation, H_2 evolution and Zn corrosion reactions occurring at the Zn electrolyte interface are challenges that need to be addressed to achieve highly stable Zn anodes as well as the long lifespan of ZIBs. From the perspectives of anode construction, separator modification and electrolyte optimization, a series of effective strategies can be summarized as follows.

3.2.1   Surface modification of Zn metal anodes

Constructing a coating layer on the surface of the Zn anode can effectively adjust the electronic and ionic field at the electrode|electrolyte interface to achieve the uniform Zn nucleation and flat Zn deposition layer at the interface, thereby improving the cycle life and interface stability of the Zn anode. According to previous reports, different Zn metal-protective layers such as inorganic coatings [113–121], metal modification layers [122–125] and organic coatings [126–128] can be constructed on the surface of Zn anodes through the *ex-situ/in-situ* method to achieve high-performance Zn anodes. It is noted that non-conductive inorganic coatings on the Zn anodes may cause an enlarged interfacial impedance and slow zinc plating/stripping kinetics. The following content briefly reviews the research progress of the above three protection layer strategies.

(1) *Ex-situ* preparation of coatings on the surface of the Zn anode

The protective layer can be constructed on the surface of the Zn anode by *ex-situ* methods, such as doctor blade coating, spin coating and physical pressing.

① Inorganic coating layer. The *ex-situ* doctor blading method is the most commonly used method to prepare a coating layer on the surface of the Zn anode. By uniformly dispersing coating materials and binders in solvents and making slurry then casting on the Zn foil, the thickness of the coating is controlled by the blade. Yi *et al*. [116] cast the ZrO_2 nanoparticle slurry onto the Zn anode to facilitate the uniform Zn stripping/plating. ZrO_2 is a typical ceramic insulating material with a high dielectric constant ($\varepsilon\sim25$), and the ZrO_2 coating underwent the Maxwell–Wagner polarization during the charge/discharge process and provided more nucleation sites for Zn^{2+}, which promoted the Zn^{2+} diffusion and ensuring a uniform Zn stripping/plating process (Figure 7a). Therefore, the Zn anode with the ZrO_2 coating can achieve a cycle life of 2,100 h at 5 mA cm^{-2} (compared with the bare Zn of 100 h) and a polarization voltage of only 32 mV (Figure 7b). Besides, the uniform deposition of Zn^{2+} can also be achieved by scraping the nitrogen and sulfur double-doped orange peel-based biomass activated carbon (NS-OPC)-based artificial protective layer on the surface of Zn foil [119]. The nitrogen-containing functional groups and sulfur heteroatoms in the NS-OPC provided nucleation sites for the uniform deposition of Zn. Consequently, the cycle life of the NS-OPC-coated Zn symmetric cell was as high as 1,200 h at a current density of 1 mA cm^{-2}.

The spin coating method can be used for the construction of the *ex-situ* layer. By adjusting the rotation speed and viscosity of the solvent, the liquid solution is evenly dispersed on the surface of the Zn anode. After solvent evaporation, a uniform film can be formed on the surface of the Zn anode. Nb_2O_5 also has a high dielectric constant and can be constructed on the surface of the Zn anode by the *ex-situ* spin coating [117]. The Nb_2O_5@Zn symmetric cell achieves stable Zn^{2+} plating/stripping up to 1,000 h at a current density of 1 mA cm^{-2}. Dong *et al*. [120] dispersed ZnO porous sheets on the water-based filter membrane by vacuum filtration and pressed it on the surface of the Zn anode. The strong hydrophobicity of ZnO porous sheets significantly alleviated the corrosion problem of the Zn anode interface, and the stability of the Zn anode was significantly improved.

② Metal coating layer. Metal materials are promising coating materials for ZIBs due to their affinity to Zn and excellent electrical conductivity. The affinity of metal materials to Zn can increase the nucleation sites of Zn^{2+} to promote the uniform deposition of Zn. In addition, the conductivity of the metal can surpass even the interfacial electric field of the Zn anode, realizing a rapid transport of Zn^{2+} which effectively suppresses the formation of Zn dendrites/protrusions [129]. Dong *et al*. [125] reported a strategy to construct a zincophilic 3D Cu nanowire network on the surface of Zn foil through an *ex-situ* manner to stabilize the Zn anode in multiple aspects. According to the experimental results, the Cu nanowire network covering the surface of the Zn anode evened the surface electric field and the Zn^{2+} concentration field of the Zn anode (Figure 7c), and its hydrophobic property also inhibited the occurrence of side reactions (Figure 7d), which helped to achieve the uniform deposition of Zn ions. Density functional theory calculation showed that the facets and edge sites (especially the latter) of Cu nanowires exhibited high zincophilicity (Figure 7e). The edge sites of Cu nanowires with incompletely coordinated atoms were highly reactive to the Zn deposition, which benefited the uniform Zn nucleation/deposition.

③ Organic coating layer. Organic molecular materials can also be used as protective coatings for Zn anodes to improve interfacial properties. Cui *et al*. [130] applied a polyamide (PA) organic polymer protective layer on the surface of the Zn anode by the *ex-situ* doctor blading method, which effectively regulated the deposition behavior of Zn. The artificial PA coating had a unique hydrogen bond network structure, which strongly coordinated with metal ions, accelerating the migration of Zn^{2+} and achieving uniform nucleation of Zn, and also inhibited the corrosion effect of H_2O/O_2 on Zn anodes (Figure 7f). The change of the current with time at a constant potential can sensitively reflect the Zn
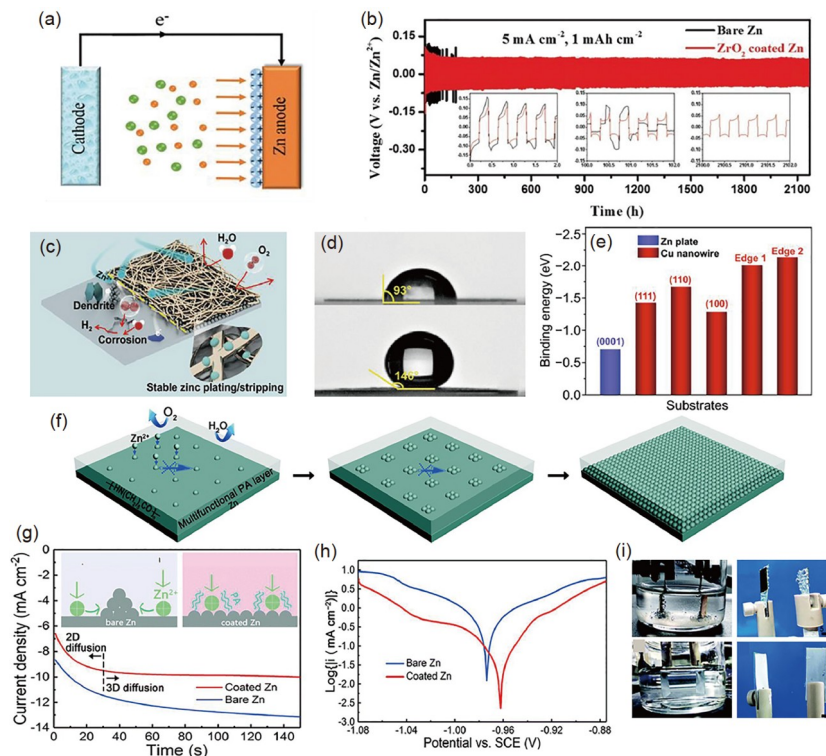
Figure 7　*Ex-situ* preparation of coatings on the surface of Zn anodes. (a) Schematic of the stripping/plating processes of the ZrO$_2$-coated Zn anode. (b) Voltage profiles of the metallic Zn plating/stripping in the Zn symmetric cell and ZrO$_2$-coated Zn symmetric cell at 5 mA cm^{-2} for 1 mAh cm^{-2} [116]. (c) Schematic illustration of protective effects of Cu nanowires on Zn anodes. (d) The water contact angle of the Cu nanowire/membrane (upper) and Zn foils (below). (e) Binding energies between the Zn atom and different substrates of Zn plates and Cu nanowires [125]. (f) Schematic diagrams for the Zn deposition on PA-coated Zn. (g) CA curves of bare Zn and PA-coated Zn at a −150 mV overpotential. (h) Linear polarization curves showing the corrosion on bare Zn- and PA-coated Zn. (i) The surface morphology of a bare Zn (upper) and a PA-coated Zn (below) plate after 100 cycles [130] (color online).

nucleation process and the change of Zn anode surface morphology by the chronoamperometry. For the bare Zn electrode, the current density continued to increase after applying −150 mV overpotential for 150 s, suggesting that its rampant 2D diffusion time on the surface was long and rough deposition propagation (the inset of Figure 7g). The initial Zn nucleation and 2D diffusion process of the Zn anode with PA protective layer was less than 30 s, followed by sustained and stable 3D diffusion. Since the PA coating was strongly adsorbed on the Zn anode, it provided an additional energy barrier for the lateral movement of Zn^{2+} adsorbed on the Zn anode interface and increased the nucleation sites, eventually evolving into a uniform and dense Zn layer. In addition, compared with bare Zn electrodes, the Zn anode with the PA protective layer had better corrosion resistance, which helped to suppress the generation of side reactions (such as hydrogen evolution reaction) at the electrode|electrolyte interface (Figure 7h). As shown in Figure 7i, the effect of the PA protective layer on the electrochemical plating/stripping of the Zn anode was visualized through a transparent electrolytic cell. It was found that the bare Zn electrode showed obvious bubbles and continuous stripping of the Zn hydroxide and zincate during the cyclic plating/stripping process, while the PA-protected Zn anode showed no bubbles and a

smooth surface throughout the cycle. Guo *et al.* [126] constructed a polyvinyl butyral film with the high viscoelasticity on the surface of the Zn anode through a simple spin-coating strategy. This protective layer had good adhesion, ionic conductivity, and mechanical strength, which can effectively block the contact of active water at the electrode|electrolyte interface and guide Zn^{2+} to platting/stripping uniformly under the polyvinyl butyral film, so the electrode containing Zn exhibits the high cycling stability and CE.

(2) *In-situ* preparation of coatings on the surface of the Zn anode

Compared with the protective layer formed *ex-situ* on the Zn anode surface, the *in-situ* formed Zn anode-protective layer does not require the addition of binders such as polyvinylidene fluoride (PVDF), and generally has stronger adhesion. So far, ZnO, ZnS, Al$_2$O$_3$, MXene, Sn, In, AgZn$_3$, and ZIF-8 have been reported to form protective layers *in situ* [113–115,118,121–124,128,131–133]. These layers are usually formed *in-situ* by anodizing technique, chemical vapor deposition, atomic layer deposition, wet chemical methods, replacement reactions, complexation reactions, and other strategies.

① Inorganic coating layer. Liu *et al.* [115] constructed a Zn hexagonal pyramid array with a functionalized ZnO layer

on the surface of the Zn anode through an *in-situ* anodizing technique and reduced the local current density on the electrode surface by increasing the electroactive surface area of the Zn anode. In addition, the functionalized ZnO coating formed on the surface of the Zn hexagonal pyramid array had a gradient thickness to achieve the long-term cycle stability of the Zn anode by guiding the selective deposition of Zn^{2+} and alleviating interfacial side reactions.

Chemical vapor deposition has the advantages of simple preparation conditions and fast preparation speed, so low melting point materials can chemically react with the Zn foil to construct an interface modification layer *in-situ*. Guo *et al.* [113] diffused sulfur vapor to the surface of Zn metal under vacuum-tight conditions and formed a dense and uniform ZnS protective layer *in-situ* through the reaction of sulfur vapor and Zn metal (Figure 8a). The thickness of the ZnS protective layer can be controlled by adjusting the treatment temperature to further optimize the performance of the protected Zn electrode. By studying the rate performance of Zn symmetric batteries at different current densities, the voltage hysteresis of bare Zn symmetric batteries was always higher than that of ZnS@Zn symmetric batteries, indicating that ZnS@Zn symmetric batteries had the low polarization and favorable stability at a high current density (Figure 8b). This dense ZnS protective layer not only acted as a physical barrier to inhibit the Zn corrosion, but also acted as an inducer for uniform Zn^{2+} plating/stripping beneath the ZnS film.

In addition to the above methods, atomic layer deposition is a new thin film deposition method in which the coating is formed by stacking and growing atoms layer by layer. Therefore, this method can precisely control the thickness of the film while achieving the uniform coverage at the atomic scale. Liu *et al.* [114] constructed an ultra-thin Al_2O_3 layer *in-situ* on the surface of the Zn anode by atomic layer deposition. This protective layer improved the hydrophilicity of the Zn anode and effectively inhibited the corrosion of Zn, and the growth of Zn dendrites was significantly inhibited and the cycle life of the Zn symmetric battery was significantly increased.

Wet chemistry is a simple, low-cost, and scalable method to grow a thin and uniform protective layer on the surface of Zn anode *in situ* through corresponding chemical reactions. Zhou *et al.* [118] prepared ZP@Zn by soaking the Zn foil in an aqueous solution containing $Zn(NO_3)_2$ and $(NH_4)_2HPO_4$ through a simple *in-situ* wet chemical reaction. The ZP layer has a reversible proton storage capacity to alleviate the hydrogen evolution reaction, and promotes the redistribution of charges under the action of an electric field through the space charge polarization effect, and the uniform nucleation and deposition of Zn. In addition, MXene can also form a thin and uniform protective layer on the surface of the Zn anode through *in-situ* spontaneous reduction/assembly [121]. The

MXene layer lowers the nucleation energy barrier of the Zn anode and uniforms the electric field distribution through the charge redistribution effect, achieving good cycle performance of the Zn anode.

② Metal coating layer. It is a simple and large-scale method to construct a uniform and dense metal layer *in-situ* on the surface of the Zn anode through the chemical displacement reaction between metal ions (such as Ag^+, Au^+, Cu^{2+}, In^{3+}, and Sn^{4+}) and Zn metal. Yang *et al.* [123] constructed a Sn layer on the surface of the Zn metal anode *in situ* through a simple chemical displacement reaction (Figure 8c). By controlling the reaction time between Zn foil and $SnCl_4$ solution, $Zn/Sn_{(101)}$ electrodes and $Zn/Sn_{(200)}$ electrodes with different crystal plane orientations can be well-prepared (Figure 8d). The nucleation over-potentials of $Zn/Sn_{(101)}$ and $Zn/Sn_{(200)}$ (9.3 mV and 16.4 mV) was much smaller than the bare Zn anode (35.9 mV), indicating that the Sn surface was more conducive to the nucleation and growth of Zn (Figure 8e). In addition, In and $AgZn_3$ can also be constructed on the surface of the Zn anode through a chemical displacement reaction [122,124]. Metallic In and $AgZn_3$-based metal protective layers can lower the Zn nucleation barrier and regulate the Zn deposition through a facile and effective method to realize long-life rechargeable aqueous ZIBs.

③ Organic coating layer. Interestingly, some organic molecules have the ability to complex with Zn^{2+}. By soaking the Zn foil in the corresponding solution, a strong adhesion organic molecular layer can be constructed *in situ* on the surface of the Zn anode through the complexation reaction. Kang *et al.* [128] used the *in-situ* complexation reaction between phytic acid and Zn foil to construct an organic zincophilic interfacial layer. Phytic acid organic molecules are composed of six phosphate groups, which have strong complexation with metal ions. The inherent surface binding affinity of phosphates helped to form a strong binding phytic acid cross-linked network structure on the surface of the Zn anode (Figure 8f). The Zn–phytic acid@Zn anode and MnO_2 cathode were subsequently assembled into a flexible Zn|MnO_2 battery. Thanks to the strong adhesion between the phytic acid and the Zn anode, the flexible device exhibited high and stable specific capacity under different bending angles (Figure 8g). The flexible device can serve as a strap for an electronic watch and power it, demonstrating the good mechanical properties of the as-grown organic layer (Figure 8h). Under folding conditions, the organic protective layer grown *in situ* was not easy to fall off and can continuously and stably protect the metal Zn anode, reflecting the practical feasibility of these flexible ZIBs. Besides, the flexible ZIBs can still drive and power an electric fan when folded 180°, indicating its potential for flexible and wearable electronics in future daily life (Figure 8i).

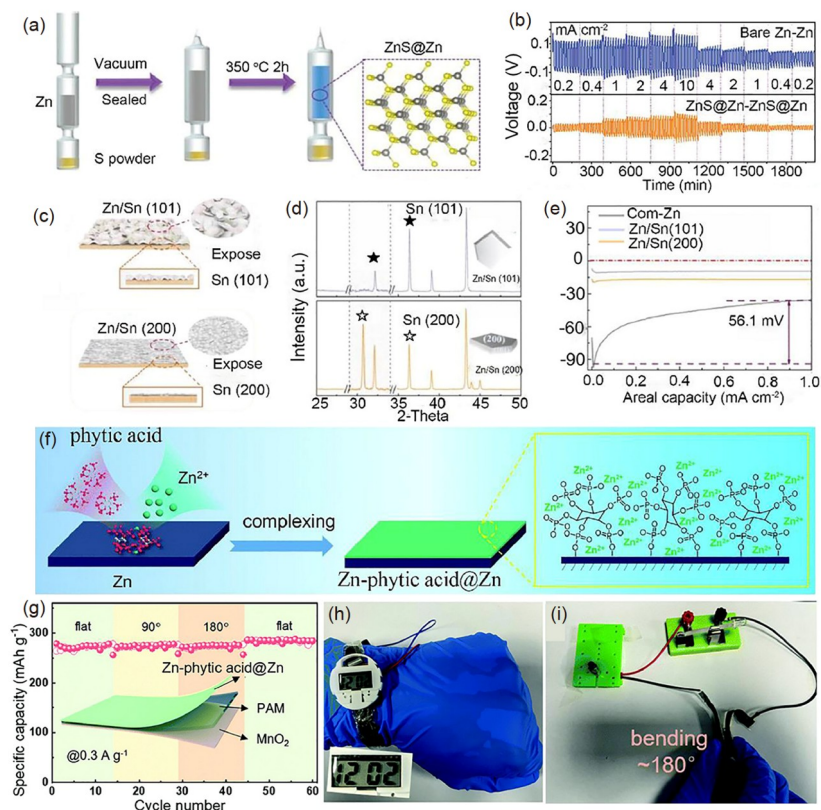Due to the unique hydrophilicity and porous surface of

Figure 8 *In-situ* preparation of coatings on the surface of Zn anodes. (a) Schematic of introducing the ZnS layer on the surface of Zn metal substrate by an *in-situ* chemical vapor deposition reaction. (b) Rate performances of bare Zn symmetric cell and ZnS@Zn-350 symmetric cell at different current densities [113]. (c) Schematic illustration of the modification process of the Zn/Sn electrodes. (d) X-ray Diffraction patterns of the Zn/Sn electrodes. (e) Voltage profiles of Zn deposition on bare Zn, Zn/Sn$_{(101)}$, and Zn/Sn$_{(200)}$ at a current density of 1 mA cm^{-2} and a capacity of 1 mAh cm^{-2} [123]. (f) Schematic illustration of the Zn–phytic acid *in-situ* coating mechanism and a diagram of the Zn–phytic acid structure on the Zn anode. (g) Cycling performance of the flexible ZIBs under different bending states. The flexible ZIB powered (h) a flexible electronic watch and (i) a fan under dynamic deformation [128] (color online).

MOF materials, a protective layer of MOF materials can be constructed *in situ* on the surface of the Zn anode by the wet chemical method. Ruoff *et al.* [127] constructed a ZIF-8 layer *in situ* on the surface of the Zn anode, followed by carbonization to obtain a Zn anode with a protective layer of N-doped porous carbon derived from ZIF-8. The good hydrophilicity and porous surface of the N-doped porous carbon layer derived from ZIF-8 helped to accelerate the diffusion of Zn^{2+} and uniform electric field distribution, thereby suppressing the formation of Zn dendrites and the generation of side reactions at the electrode|electrolyte interface.

3.2.2   Alloy anodes and zinc-metal free anodes.
Compared to pure Zn anode, the formation of the intermetallic phase in alloy anodes results in a significantly positive corrosion potential, strong antioxidant capability and low Zn-nucleation barrier [131]. Therefore, the replacement of pure Zn metal by an alloy anode is expected to improve the cycling stability of ZIBs by inhibiting the formation of Zn dendrites and side reactions.

For example, Jiang *et al.* [134] reported a eutectic Zn$_{88}$Al$_{12}$ alloy with unique layered nanostructures alternating Zn and Al as a new anode. The forming and insulating Al$_2$O$_3$ shell prevented the electroreduction of Zn^{2+} ions, thus guiding its Zn-deposition sites and greatly eliminating the formation of Zn dendrites, while Al inhibited the formation of irreversible ZnO or Zn(OH)$_2$ by-product. Benefiting from the unique structure and protection of the Al/Al$_2$O$_3$ core/shell, the Zn$_{88}$Al$_{12}$ alloy exhibited the superior Zn plating/stripping behavior up to 2,000 h, as shown in Figure 9a. Researchers demonstrated experimentally and computationally that HER occurring in the alloy anode with the moderate Sn amount is only half that of the bare Zn anode [135]. Compared with pure Zn (001), the replacement of Zn atoms with Sn metal atoms could possibly enlarge the Gibbs free energy of H at the adsorption sites in the ZnSn (001) alloy and inhibit the HER. In addition, theoretical calculations pointed out that the zincophilic Sn doping atoms can reduce the Zn deposition energy barrier to drive the heterogeneous nucleation of Zn on the electrode surface, thus inhibiting the formation of Zn dendrites [135]. Another alloy material of electrodeposition-synthesized Zn$_5$Cu possess a forest-like three-dimensional nanostructure. The surface of the three-di-
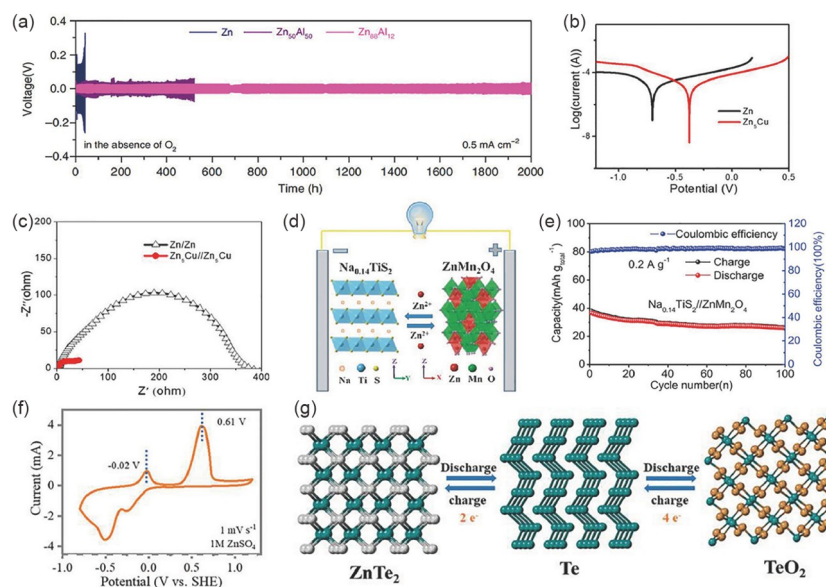
Figure 9 Design principle and electrochemical performance of alloy anodes. (a) Long-term cycling of symmetric batteries of Zn, $Zn_{50}Al_{50}$ or $Zn_{88}Al_{12}$ anodes at 0.5 mA cm^{-2} [134]. (b) Tafel plots of Zn and Zn–Cu anodes. (c) Electrochemical impedance spectroscopy of Zn‖Zn and Zn–Cu‖Zn–Cu cells [136]. (d) Structural illustrations and (e) cycling performance of $Na_{0.14}TiS_2|ZnMn_2O_4$ Zn-ion full batteries [141]. (f) CV curves of Te under the three-electrode test. (g) Schematic model of phase transformation during the (dis)charging [144] (color online).

mensionally nanostructured Zn/Cu alloy has been demonstrated to be in favor of accelerating the reaction kinetics and improving the corrosion-resistant ability of Zn anodes (Figure 9b, c) [136]. Besides the aforementioned Zn/Al, Zn/Sn and Zn/Cu alloys, Zn depositing on other Zn-based alloys such as Zn/Au, Zn/Ag and Zn/In also exhibits notably reduced nucleation energy barriers [137]. Generally, the optimization mechanism of Zn plating/stripping by alloy anodes can be summarized as follows [135,136,138]: (1) the alloys (*e.g.*, Zn/Ag) featuring the high lattice matching degree with Zn can adjust the Zn deposition orientation; (2) the alloys (*e.g.*, Zn/Cu) with the zincophilic feature reduce the Zn nucleation barriers, thus suppressing rampant Zn^{2+} diffusion at the anode–electrolyte interface and realizing the dense Zn deposition; (3) the alloys (*e.g.*, Zn/Sn) which are antipathetic to protons benefit to inhibit the HER reaction.

Dendrite growth and side reactions of Zn metal anodes seriously affect the cell performance, and even cause safety problems. Especially, the above issues become more serious when the Zn anodes work under a large charge/discharge depth (*i.e.*, high utilization). That is, Zn anodes often operate under low utilization. Because of the low utilization, excess Zn metal must be used in Zn-based energy storage systems, which seriously damages the energy density of the whole device [139].

Looking back at the history of LIBs, an effective solution to the above challenges is the development of metal-free batteries. Especially, the formation of Zn dendrites is effectively eliminated in intercalation-type or conversion-type anode whose potential of the Zn-inserting or conversion re-

action is often higher than the Zn reduction potential, thus significantly improving the cycling stability of ZIBs. Hong *et al.* [140] reported Zn^{2+} ions inserted in $Zn_xMo_6S_8$ Chevrel phases at a low voltage of 0.35 (Zn^{2+}/Zn) and exhibited low cell volume changes during the charging and discharging. In addition, presodiated TiS_2 was used as a new anode for ZIBs, in which the buffer phase formed improved the reversibility and stability of the structure [141]. As a result, the "rocking-chair" ZIBs configured with a $Na_{0.14}TiS_2$ anode and a $ZnMn_2O_4$ cathode provided an average voltage of 0.95 V and capacity retention of 74% after 100 cycles (Figure 9d and e). Layered materials such as MoO_3 [142] and $NaTi_2(PO_4)_3$@C [143] have also been used as the anode for "rocking-chair" ZIBs due to their low Zn-embedding potential and high electrochemical stability.

However, the unsatisfactory electrochemical performance of these anodes can be ascribed to insertion mechanisms that provide relatively low specific capacities and unstable output voltages. By contrast, conversion-type anodes with high specific capacities and flat voltage plateaus showed great potential for building high-performance ZIBs. As shown in Figure 9f and g, the non-metallic Te anode provided a significantly high theoretical capacity of 425 mAh g^{-1} and a stable output voltage during the conversion process of Te to $ZnTe_2$ to ZnTe in a neutral electrolyte [144]. The Te|MnO$_2$ full batteries coupled with such Te anodes achieve energy densities of up to 81 Wh kg^{-1}$_{anode+cathdoe}$ and superior cycling behavior of 5,000 cycles in mild electrolytes, and even more excellent electrochemical performance in alkaline electrolyte systems (*e.g.*, 176 Wh kg^{-1}$_{anode+cathdoe}$). Cu_{2-x}Se [130] and

$Cu_{2-x}Te$ [145] anodes based on the conversion mechanism similarly released low and flat discharge voltages and excellent cycling stability, conferring promising practical applications for "rocking-chair" ZIBs.

3.2.3 Anode-free Zn-ion batteries

Most of the current studies use the Zn foil, Zn powder, or electrodeposited Zn as an anode with the low Zn utilization. Achieving high energy-density ZIBs requires a reduction of the battery N/P ratio as much as possible. Cui *et al.* [146] proposed the concept of an anode-free ZIB, which omitted the Zn metal anode and the internal Zn source was stored at the cathode (*i.e.*, the "real Zn anode" was formed when the battery was first charged). This battery configuration significantly reduced the internal volume/mass compared to conventional ZIBs and thus increased the energy density of the whole battery. Due to the very limited internal Zn source, the Zn plating/stripping CE required >99.7%.

Interfacial modification can effectively suppress dendrites and HER to improve the Zn plating/stripping reversibility and extend the cycle life of anode-free ZIBs. Wang and his colleagues [147] coated aluminum fluoride on the copper foil (Cu@AOF) as a substrate for the Zn deposition in anode-free ZIBs. As shown in Figure 10a, the strong interaction between AOF and Zn^{2+} significantly reduced the Zn nucleation and growth barriers (Figure 10b), achieving highly reversible Zn plating/stripping with a CE of 99.78% even at −20 °C. The Cu@AOF‖$Zn_{0.5}VO_2$ anode-free full battery showed a long cycle life of 400 cycles. In addition, 2D Sb/Sb_2Zn_3 alloy heterostructures were designed at the interface to regulate the Zn plating [148]. Strong adsorption and homogeneous electric field distribution in the Sb/Sb_2Zn_3 heterostructure interface appeared during the Zn plating process (Figure 10c), which endowed the Zn metal with the high stability

even at ultrahigh current densities (*e.g.*, CE of 98.3% at 50 mA cm^{-2} and 50 mAh cm^{-2}) and indicated excellent application potential in high-power Zn batteries such as anode-free Zn‖Br_2 batteries with a high-rate capability (Figure 10d).

Optimizing the electrolyte formula makes it possible to achieve the dendrite-free Zn plating/stripping with a high CE. Wang *et al.* [149] reported an aqueous Zn-ion battery in which an aqueous electrolyte with an alkylammonium salt additive contributes to the in-situ formation of SEI. As shown in Figure 10e, the robust SEI on the Zn anode with superior Zn^{2+}-conductive and water-resistant capability achieved dendrite-free plating/striping and long-term cycling behavior of 6,000 h in a Zn|Zn symmetric cell with 99.9% CE and also allowed the anode-free pouch cell of Ti‖Zn_xVOPO_4 to operate reversibly for 100 cycles at 100% depth of the discharge. Qian's group [150] designed a stable F-rich SEI by introducing a multifunctional ZnF_2 additive into the electrolyte. This ZnF_2 interfacial layer not only regulated the growth direction of Zn metal, but also acted as an inert protective layer to prevent the generation of side reactions such as H_2. The optimized electrolyte enabled the anode-free Zn-ion battery to significantly improve the cycle life accompanied with a high CE.

Normally the formation of Zn dendrites and HER are associated with the involvement of water in the Zn^{2+} solvation structure ($Zn(H_2O)_6^{2+}$), and the exclusion of water molecules from the solvation structure can effectively solve these problems, especially for HER. The addition of chloride salts with bulky cations (1-ethyl-3-methylimidazolium chloride) to the conventional $ZnSO_4$ electrolyte successfully transformed $Zn(H_2O)_6^{2+}$ into anhydrous solvation structure of $ZnCl_4^{2-}$ [151]. The unique solvation structure of $ZnCl_4^{2-}$ with weakening cation–water interactions effectively inhibited the formation of HER and Zn dendrites. The opti-
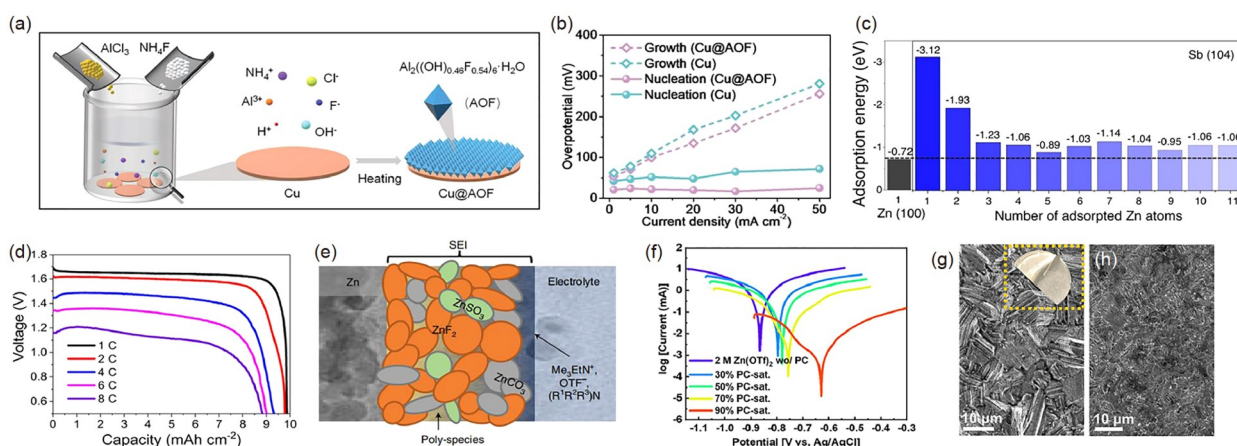

Figure 10 Design principle and electrochemical performance of anode-free ZIBs. (a) Schematic illustration of the preparation process of Cu@AOF. (b) Nucleation overpotential of Zn|Cu cells at different current densities [147]. (c) Adsorption energy of the Zn atoms on Zn (100) and Sb (104) crystal planes. (d) Discharge curves of anode-free Zn‖Br_2 batteries at different current densities [148]. (e) Cartoon of the Zn^{2+}-conducting SEI [149]. (f) Tafel plots of Zn in three-electrode configuration. Morphological evolution of the Zn anodes in the 50% PC-sat. electrolyte: (g) the first plating and (h) the 100th stripping [152] (color online).

mized electrolyte achieved uniform Zn plating with an average CE of 99.9% and thus resulting in an anode-free ZIB with a capacity retention of 78.8% after 300 cycles. Anion-driven inorganic SEI allows the metal anode to exhibit excellent cell electrochemical properties, but it is difficult for the vast majority of anions to enter the Zn^{2+} solvent sheath structure and to be reduced before Zn^{2+} and H_2O for their higher lowest unoccupied molecular orbital levels. In the presence of propylene carbonate-saturated electrolyte (denoted as PC-sat.), the trifluorate anion participates in the Zn^{2+} solvent sheath structure even at low salt concentrations, whose unique solvent structure leads to the reduction of the anion and results in the formation of a hydrophobic SEI [152]. The waterproof SEI and the reduction of water activity in the mixed electrolyte effectively prevented side reactions (Figure 10f), thus ensuring a dendrite-free Zn deposition/exfoliation with the unprecedented CE over 99.93% (Figure 10g, h) and anode-free Zn-ion batteries with superior cycling stability (*e.g.*, 80% capacity retention after 275 cycles).

3.2.4　Functional separators

The modification of conventional separators and the development of novel separators have recently emerged as effective routes to manipulate the Zn^{2+} ion transport and Zn deposition behaviors, thus improving the electrochemical stability of Zn anodes. It has been proved that separators with uniform pore sizes are beneficial to the homogenization of ion flux and reduce the accumulation of Zn^{2+} at the Zn deposition interface. Wang *et al*. [153] proposed a porous water-based filter membrane as a separator due to its better toughness and uniform pore distribution compared with commercial glass fiber (GF) separators. The lifespan of the symmetrical cell using a filter membrane received is over 2,600 h with a low voltage hysteresis of 47 mV. For those separator substrates without a homogeneous pore structure, it can also play a role in the homogeneous ion flux by introducing functional materials, such as MOF, with the homogeneous pore structure. For instance, a Janus separator containing both Zn-ion-conductive MOF and rGO was proposed, which was able to regulate the uniform Zn^{2+} flux and electron conduction simultaneously during the battery operation [154]. A separator (UiO-66-GF) modified by the Zr-based MOF *via* a hydrothermal method was proposed by He *et al*. [155]. The large specific surface area and abundant pore structure of UiO-66-GF provided the high transport ability for charge carriers at the separator–electrolyte interface.

Introducing functional groups and other zincophilic sites into the separator is a typical strategy to equalize the Zn^{2+} ion flux, limit the anion movement, increase the Zn^{2+} transfer number, reduce the concentration polarization at the Zn deposition interface, and inhibit the side reactions. A Janus separator was constructed *via* parallelly grown graphene

sheets modified with sulfonic cellulose on one side of the GF separator through the spin-coating technique (Figure 11a). The crystallographic orientation of Zn and Zn^{2+} transference speed can be simultaneously optimized by the Janus separator (Figure 11b) [156]. For the PVDF@polydopamine-functionalized nanofibrous separator, the functional groups (–OH and –NH–) in polydopamine facilitated the formation of Zn–O and Zn–N based on the metal–polydopamine coordination chemistry, homogenizing the Zn-ion flux and thus enabling the dendrite-free Zn deposition. At the same time, the PVDF@polydopamine separator prevented the V-species from shuttling through the separator due to the strong V–O bond interaction. Therefore, the rate capability and cycling stability of the $Zn|NH_4V_4O_{10}$ batteries were significantly improved with a capacity retention of 92.3% after 1,000 cycles at 5 A g^{-1} [157]. Cotton-derived cellulose films with abundant hydroxyl groups, outstanding mechanical properties, and large ionic conductivity, can increase the Zn ion transfer number, lower the desolvation barrier of hydrated Zn ions, thus reducing the Zn nucleation overpotential and accelerating the Zn deposition kinetics [158]. Benefiting from the $BaTiO_3$ decoration with high zincophilicity anchoring on GF as well as filling the surface gap of the separator, the dual-interface engineering-modified separator can not only effectively capture and accelerate Zn^{2+} transport between the fiber–electrolyte interface, but also redistribute the ion transport into the homogenization in the separator|anode interface [159]. As a result, the cumulative capacity of Zn|Zn cells maintained up to 9,500 mAh cm^{-2} at the high current density of 10 mA cm^{-2}.

The construction of a conductive surface on one side of the separator is helpful in avoiding the formation of a large local current density at the Zn anode/separator interface. Liu *et al*. [160] developed a Janus separator *via* directly growing vertical graphene (VG) containing oxygen and nitrogen heteroatoms on one side of a commercial GF separator through plasma-enhanced chemical vapor deposition (PECVD) and a simple air plasma treatment (Figure 11c). Figure 11d exhibits the top-view scanning electron microscopy (SEM) image of the VG carpet, which consists of VG-wrapped GF with each other. High-magnification observation (inset of Figure 11d) further proves that uniform and interconnected VG arrays derived from PECVD completely covered the surface of GF with affording the carpet-like morphology. The symmetric cell using the Janus separator maintained a durable lifespan of 600 h under a high current density of 10 mA cm^{-2}. The 3D-conductive VG layer provided the sufficient surface area, porous architecture, and zincophilic nature from the effect of oxygen and nitrogen heteroatoms. The local current density at the side of the Zn anode was reduced, thereby guaranteeing uniform Zn plating/stripping with a high reversibility.

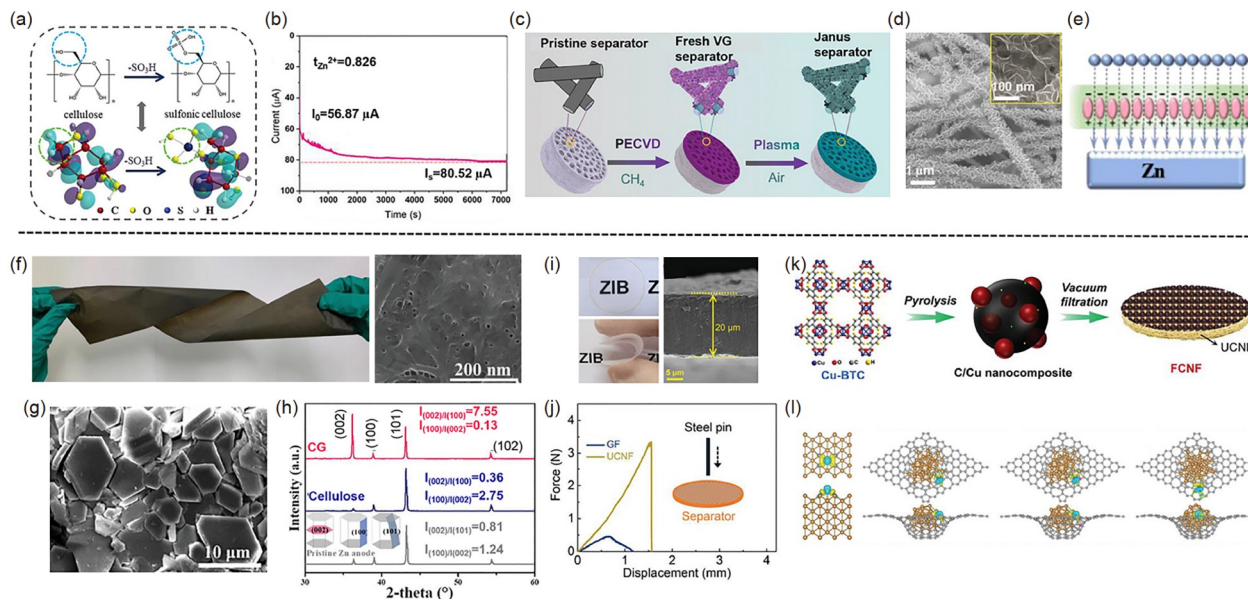High-dielectric-constant materials mingled in separators

Figure 11 Structural design and physicochemical characterization of functional separators. (a) Schematic illustration of sulfonic cellulose by grafting sulfonic acid groups on the cellulose backbone. (b) Zn^{2+} transference number of the Janus separator [156]. (c) Schematic illustration of the fabrication process. (d) Top-view SEM images of the GF@VG separator [160]. (e) Schematic illustration of the possible migration process of Zn^{2+} when passing through the ZrO_2-mixed cellulose separator [161]. (f) Photograph (left) and SEM image (right) of CG separators. (g) SEM images of Zn anode surface after cycling at 2 mA cm^{-2} with CG separators. (h) *Ex-situ* XRD patterns of Zn anodes after cycling [162]. (i) Photographs and cross-sectional SEM image. (j) Penetration force-displacement curves (the inset shows testing schematics). (k) Fabrication schematics of the double-layer functional ultrathin separators. (l) DFT calculations: differential charge densities of one zinc atom bonded at Cu, the C/Cu interface, the N-doped C/Cu interface, and the O-doped C/Cu interface (upper, top view; lower, side view), respectively [163] (color online).

would regulate Zn^{2+} transport pathways through the Maxwell–Wagner polarization mechanism under the applied electric field to realize the uniform Zn deposition and also repel anions to restrain the generation of side products. For example, Huang *et al.* [161] mixed ZrO_2 particles into a polymethyl cellulose dispersion solution and then poured the above-mentioned solution on the substrate for the dehydration. The electrolyte uptake of the prepared separator was 379%, which is higher than that of pure cellulose separators. The ZrO_2 particles with a high dielectric constant (ε=25) were subjected to the Maxwell–Wagner polarization (interfacial or space charge polarization) by an applied electric field. The electric dipole then created a polarizing electric field on the surface around the ZrO_2 particles, which rendered considerably uniform ion pathways, thus ensuring the uniform Zn deposition and motivating the fast ion diffusion kinetics (Figure 11e). In addition, components that can induce planar Zn deposition are introduced into the separators to regulate the Zn nucleation deposition behavior and hinder the growth of Zn dendrites. Wu *et al.* [162] developed a functional separator composed of cellulose nanofibers and graphene oxide (CG) to stabilize Zn anodes. The electrolyte uptake of the CG separator is 575%. This CG separator with negative surface charges and abundant zincophilic oxygen groups ensured the strong interaction between the separator and zinc species, simultaneously inducing the Zn(002) deposition due to the low mismatch between Zn(002) and GO

(002), thus initiating the preferential orientation of the Zn growth along the horizontal direction due to strong Zn binding ability, and uniform interfacial charge of Zn(002) deposition (Figure 11f–h).

However, the widely used separators in ZIBs such as conventional GF membranes and non-woven fabrics usually possess a large thickness of hundreds of micrometers, and the aforementioned modified separators are often designed based on thick GF membranes. By contrast, the thickness of commercial separators for LIBs is generally smaller than 25 μm. The thick separators in ZIBs extend the ion-transport distance and magnify the battery internal resistance, resulting in unfavorable rate performance for ZIBs. Therefore, the use of functional thin separators is also a core technique, which can save costs and improve the volumetric energy density of the battery by replacing the traditional thick and expensive separator. Our team designed 23 μm-thick functional ultrathin separators (FUSs) with outstanding electrochemical stability of Zn anodes and long-term durability [163]. The FUSs were composed of a mechanically-strong cellulose nanofiber membrane substrate and a zincophilic site-rich C/Cu nanocomposite decoration layer. In detail, a 20 μm-thick ultrathin cellulose nanofiber membrane substrate (denoted as "UCNF") with a flat and transparent surface and flexible feature was prepared (Figure 11i). The UCNF membrane displayed outstanding mechanical properties. The tensile strength and Young's modulus of the UCNF membrane were

121 MPa and 6.5 GPa, respectively, notably higher than that of the GF membrane. Moreover, the puncture strength of the UCNF membrane was 6.3 times higher than that of the GF membrane (Figure 11j). C/Cu nanocomposite decoration layers were synthesized by the thermal decomposition of Cu MOF precursors (Figure 11k), whose hydrophilic and porous features endowed the double-layer functional ultrathin separators with an electrolyte uptake of 195%. The mechanism of the C/Cu nanocomposite decoration layer in manipulating the Zn deposition interfacial chemistry was revealed by DFT calculations. The results showed that there were abundant zincophilic sites in the C/Cu nanocomposite, including the exposed surface of the Cu nanoparticles, the C/Cu interfaces (especially in the presence of N/O heteroatom) and N doping sites on the carbon carriers. (Figure 11l). In general, CNF membrane substrates of appropriate thickness, such as 20 μm, realized a good balance between the mechanical strength and ion transport resistance, with the good dendrite resistance. The high specific surface area and rich zincophilic site of the C/Cu nanocomposite decorative layer can reduce the local current density of the functional ultra-thin separators, induce uniform Zn nucleation, and accelerate Zn deposition kinetics. Therefore, the functional ultrathin separators regulated the Zn deposition interface chemistry in multiple dimensions and inhibited the formation of Zn dendrites. Studies on other types of separators, such as polyacrylonitrile-based separators with a thickness from 30–69 μm), Sn layer-coated cellulose membrane separators with a thickness of 30 μm, Nafion-coated Celgard 3501 separators with a thickness of 25 μm, and bamboo or bacterial cellulose separators have also achieved good results in stabilizing Zn anodes, and improving the electrochemical performance of the ZIBs [163–170].

3.2.5 *Electrolyte optimization*

The electrolyte is regarded as the blood of the batteries and displays an important influence on the performance of batteries. In aqueous ZIBs, the introduction of functional electrolyte additives has been developed to address the issues on Zn dendrites, H_2 evolution, and Zn corrosion reactions. Multifunctional electrolyte additives can have many effects on interface reaction, ion movement, solvation structure, hydrogen interaction, storage mechanism, and so on [171–174]. Herein we mainly review the regulatory effects of hybrid electrolytes and electrolyte additives on the Zn|electrolyte interface, including the electrostatic shield layer, adsorption layer, *in-situ* formation of SEI, and regulation of Zn^{2+} solvation clusters.

It is known that Li metal batteries have the advantage of self-passivation by the corrosion, while Zn metal cannot generate a dense SEI on its surface in the aqueous electrolyte. Hence, it is reasonable to build an appropriate SEI layer at the interface of the Zn anode and electrolyte for uniforming

the Zn ion flux [175,176]. Luo *et al.* [175] *in-situ* constructed a multifunctional composite interface (denoted as ZCS) composed of $Zn_3(PO_4)_2$ and ZnF_2 (ZCS) on the Zn anode through a chemical strategy induced by the KPF_6 additive (Figure 12a, b). In detail, the ZCS layer was easily built through a spontaneous chemical reaction between the fresh Zn metal and reactive acidic compounds derived from the decomposition of PF_6^- under a suitable content of 0.05 mol L^{-1} KPF_6. The $Zn_3(PO_4)_2$ with the high interface energy proved by the DFT calculation could suppress the Zn dendrite growth effectively, meanwhile ZnF_2 could accelerate the kinetics of Zn^{2+} transference and deposition proved by a series of electrochemical methods, and then the ZCS layer can improve the interface deposition and electrode kinetics comprehensively. Therefore, the Zn|Zn symmetric cells with ZCS–Zn could maintain the stability for more than 800 h and retain a low overpotential of about 50 mV during plating/stripping processes at a current density of 5 mA cm^{-2}, and an areal capacity of 10 mAh cm^{-2} (Figure 12c).

Apart from above mentioned inorganic salt electrolyte additives, numerous organic electrolyte additives have also been reported to regulate the Zn deposition interface and inhibit side reactions. For instance, a cationic surfactant-type electrolyte additive tetrabutylammonium sulfate (TBA_2SO_4) was proposed to stabilize the Zn anode. TBA^+ ions are electrostatically and intelligently adsorbed on the surface of the Zn anode surface, regulating the formation of the initial nucleus and shielding the hydrated Zn^{2+} ions in the electrolyte, resulting in the dendrite-free homogeneous Zn deposition (Figure 12d) [177]. In addition, the strategy only needs to add 0.029 g L^{-1} additives to achieve uniform Zn deposition. The Zn|Zn symmetric cells using 3D-Zn anodes with the TBA_2SO_4 electrolyte can cycle stably for over 456 h under 5 mA cm^{-2}, and 2 mAh cm^{-2}. Moreover, six water molecules and one Zn^{2+} in the electrolyte formed a stable solvation structure, and the solvation energy between Zn^{2+} and water can be reduced by changing the solvation structure of Zn^{2+} with the addition of electrolyte additives, to improve the reversibility of Zn [178]. Qiao *et al.* [178] developed a dual-function electrolyte additive of ethylene diamine tetraacetic acid tetrasodium salt (Na_4EDTA). They find that EDTA anions can be adsorbed on the surface of Zn metal, controlling the active site of H_2 production and inhibiting the activity of water (Figure 12e). Additionally, adsorbed EDTA promoted the desolvation of $Zn(H_2O)_6^{2+}$ by removing water molecules from the solvation sheath of Zn^{2+}. Side reactions and dendrite growth were suppressed by using the additive. The average CE of the Zn–Cu cell with optimized pH-equivalent EDTA-containing electrolyte can be up to 99.5%, confirming that the combination of EDTA anion and pH regulation synergically improved the cycling performance of the Zn anode [178,179,181–183]. Wang's team [179] *in-situ* construct a Zn anode-self-healing-protective film induced by
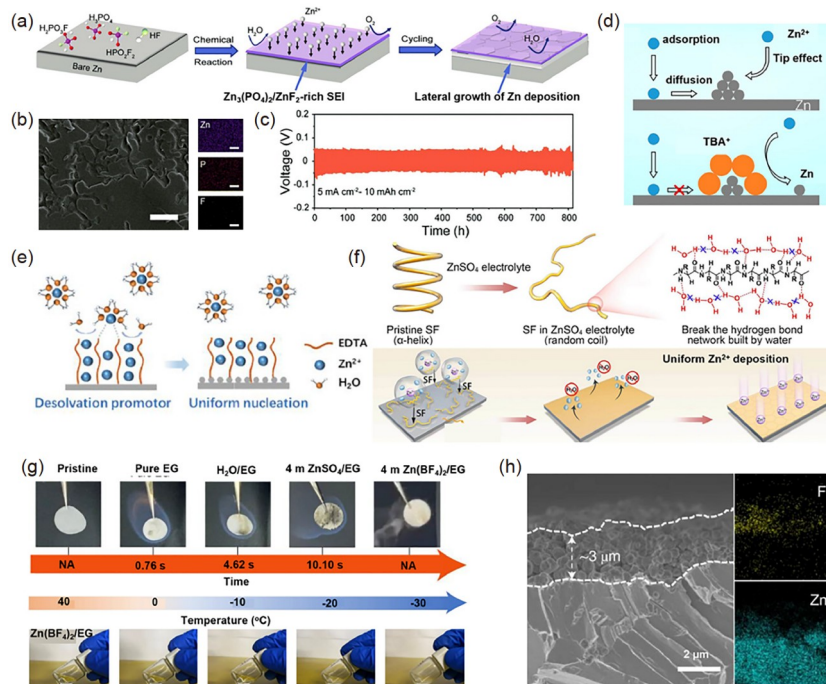
Figure 12 Optimization of electrolytes and their durability to Zn anodes. (a) Schematic illustration of the *in-situ* formation process of the ZCS interphase and its effect on the Zn deposition. (b) SEM image and elemental mappings of the Zn anode rested for 48 h in aqueous Zn|Zn symmetric cells with 0.05 mol L^{-1} KPF_6. (c) Cycling performance of symmetric Zn|Zn cells using ZCS–Zn under 5 mA cm^{-2}, and 10 mAh cm^{-2} [175]. (d) Schematics of the Zn^{2+} ion diffusion and reduction processes on electrodes in 2 mol L^{-1} $ZnSO_4$ electrolyte (upper part) and 2 mol L^{-1} $ZnSO_4$ electrolyte with 0.05 mmol L^{-1} TBA_2SO_4 (lower part) [177]. (e) Corresponding schematic illustrating the impact of EDTA on desolvation [178]. (f) Illustration of the secondary structural transformation of SF molecules and the breaking of the hydrogen bond network between water molecules (upper) and schematic diagram of Zn^{2+} ion deposition behaviors in aqueous electrolytes with SF additives (lower) [179]. (g) Ignition tests of a pristine GF separator, one saturated with pure EG, a H_2O/EG solution, a 4 mol L^{-1} $ZnSO_4$/EG solution; and optical photographs of a 4 mol L^{-1} $Zn(BF_4)_2$/EG solution (upper) and the 4 mol L^{-1} $Zn(BF_4)_2$/EG electrolyte at temperatures from 40 °C to −30 °C. (h) Cross-sectional SEM image of the Zn soaked in the 4 mol L^{-1} $Zn(BF_4)_2$/EG electrolyte for 7 days and the corresponding EDX maps [180] (color online).

a silk fibroin (SF) electrolyte additive. When 0.5 wt% SF is added to 1 mol L^{-1} $ZnSO_4$ electrolyte (denoted as $ZnSO_4$ +0.5SF electrolyte), the $ZnSO_4$ electrolyte induced the secondary structure transformation of SF molecules from α-helical structure to random coil structure. Subsequently, random coils with abundant amino and carbonyl groups were easy to form hydrogen bonds with water molecules, effectively weakening the hydrogen bond interaction between free water molecules, and participating in the solvation structure of the Zn^{2+} ion. After that, the SF molecules released from the $[Zn(H_2O)_4(SF)]^{2+}$-solvated sheath gradually adsorbed on the surface of the Zn anode and *in situ* formed a water-stable and self-healing protective film (Figure 12f). The Zn|Zn symmetric cell performed an outstanding cycling performance over 500 h even under a harsh testing condition (10 mA cm^{-2} and 5 mAh cm^{-2}). More importantly, the full battery with the potassium vanadate cathode and Zn anode showed the excellent cycling stability over 1,000 cycles at 3 A g^{-1} using the $ZnSO_4$+0.5SF electrolyte. However, in theory, the self-ionization of water cannot be restrained by limited additives. Therefore, a series of studies have been conducted on the design of nonaqueous/aqueous hybrid electrolytes, such as constructing a local hydrophobic layer

by *N,N*-dimethylformamide/H_2O, regulating the solvent structure by the electrolyte of triethyl phosphate (TMP)/H_2O, and increasing the electron density of the water protons to suppress the water activity using dimethylacetamide/TMP/ H_2O [184–186]. Moreover, as a breakthrough in the current aqueous battery path, our team recently reported a low-cost hydrous organic electrolyte, including a hydrated $Zn(BF_4)_2$ salt and an ethylene glycol (EG) solvent [180]. The synthesized 4 mol L^{-1} $Zn(BF_4)_2$/EG solution showed excellent non-flammability. The low temperature performance of the 4 mol L^{-1} $Zn(BF_4)_2$/EG electrolyte was tested. The 4 mol L^{-1} $Zn(BF_4)_2$/EG electrolyte maintained good fluidity at temperatures as low as −20 °C (Figure 12g). A cross-sectional SEM image of the Zn immersed in the 4 mol L^{-1} $Zn(BF_4)_2$/ EG electrolyte for 7 days showed that a uniform passivation layer with approximately 3 μm thickness formed on the soaked Zn surface. In addition, energy-dispersive X-ray spectroscopy (EDX) mapping exhibited that the layer was composed of F and Zn (Figure 12h), which proved the *in-situ* formation of a favorable ZnF_2 passivation layer for regulating the Zn deposition. The key to this work is the coupling of the flame-retardant hydrated $Zn(BF_4)_2$ and the low toxicity EG as a low-cost and non-flammable hydrous organic elec-

trolyte for ZIBs with enhanced sustainability.

The impact of pH on the anode plays a key role in the battery performance. On the one hand, a decrease in pH value results in the aggravated hydrogen evolution and interface corrosion. On the other hand, an increase in pH leads to an increased concentration of hydroxide ions, inducing a formation of passivation products such as zinc hydroxide sulfate and shortening the calendar life [187]. Therefore, regulating the pH of the electrolyte possesses a profound effect on improving the anode stability.

4   Other aqueous multivalent-ion batteries

In addition to the booming aqueous ZIBs, other multivalent ions such as Ca^{2+}, Mg^{2+} and Al^{3+} have also been used to develop AMBs due to their high earth abundance, intrinsic safety, relatively low redox potential (Ca/Ca^{2+}: −2.87 V; Mg/ Mg^{2+}: −2.36 V; Al/Al^{3+}: −1.68 V *vs.* SHE) and high bulk energy density [188].

Compared to Mg^{2+} and Al^{3+}, Ca^{2+} has a relatively low charge density, which provides a relatively low polarization intensity and a faster kinetic process in the host material owing to its lower charge-to-size ratio [189]. Nevertheless, few studies have been reported on CIBs. One of the main challenges is that the plating and stripping of Ca^{2+} on Ca metal anodes in conventional organic electrolytes is very difficult due to the huge resistance to the Ca^{2+} diffusion by the organic-rich phase of SEI. Wang *et al.* [190] designed a novel aqueous CIB system consisting of highly concentrated hydrogel electrolytes to replace organic electrolytes, a sulfur-containing anode to replace Ca metal anodes, and a high-voltage metal oxide cathode. The synergistic effect of high $Ca(NO_3)_2$ salt concentration and polyvinyl alcohol (PVA) strongly inhibited the water activity in the gel electrolyte, thus allowing an expanded electrochemical stability window for the sulfur–calcium polysulfide conversion chemistry (Figure 13a). Meanwhile, the *in-situ* electrochemically synthesized $Ca_{0.4}MnO_2$ cathode exhibited highly stable Ca^{2+} intercalation/deintercalation, and the developed all-calcium/ sulphur cell delivered a high specific energy of 110 Wh kg^{-1}, with stable cyclability and excellent safety under abusive conditions (Figure 13b). The main challenge on the cathode side lies in the lack of suitable electrode materials due to the large size of Ca^{2+} (~100 pm). Prussian blue analog (PBA) is a metal-organic backbone with a sufficiently large open channel structure that is expected to accommodate Ca^{2+} transport and diffusion, which has also been successfully applied to other aqueous multivalent metal-ion batteries [191]. Meanwhile, the development of anode materials is sporadic in the existing literature, with most of the available reports based on organic anodes. Mitra *et al.* [192] investigated polyaniline (PANI) as an anode for an aqueous
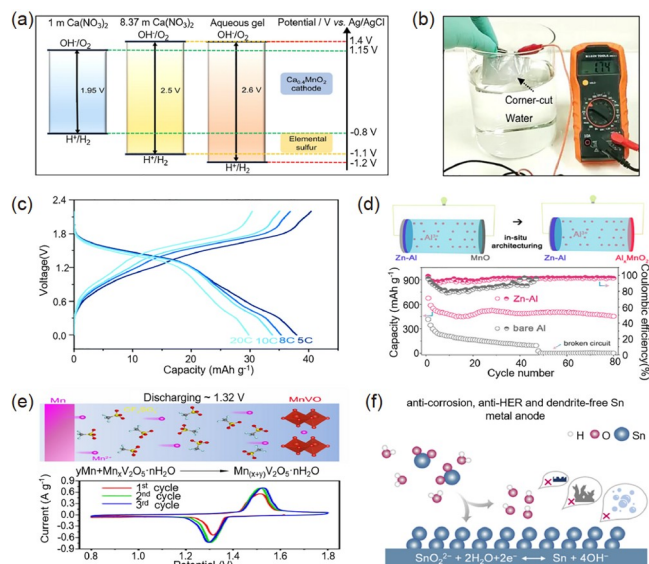

Figure 13 Design Strategies for other aqueous multivalent-ion battery systems. (a) Electrochemical stability windows of different aqueous electrolytes, and the redox voltages of the $Ca_{0.4}MnO_2$ cathode and sulfur anode obtained from experimental data [190]. (b) Water-soaking test of the charged S/C|aqueous gel electrolyte|$Ca_{0.4}MnO_2$ pouch cell after corner cut [190]. (c) Galvanostatic charge–discharge curves of a full MIB based on the hydrated eutectic electrolyte [198]. (d) Cycling performance comparison of metal|Al_xMnO_2 full cells using different anodes in 2 mol L^{-1} $Al(OTF)_3$ electrolyte at a current density of 100 mA g^{-1} [200]. (e) Schematic diagram of the discharging mechanism of $Mn|Mn_{0.18}V_2O_5 \cdot nH_2O$ cells and CV curves of the Mn|*tetra*-chloro-benzoquinone cell at 0.2 mV s^{-1} [202]. (f) Schematic illustration of Sn plating from the electrolyte of KOH with SnO_2^{2-} [203] (color online).

CIB, where potassium hexacyanoferrate was chosen as the cathode. As a result, the PANI/carbon cloth (CC) anode exhibited an impressive specific capacity of 130 mAh g^{-1} and a high capacity was still maintained after 200 cycles at 0.8 A g^{-1}. In addition, small molecule organic crystals [193] and doped metal oxides [194,195] were also proven to be useful anode candidates to improve the cycling stability and specific capacity of aqueous CIBs.

Slow solid-state diffusion and insufficient ionic conductivity due to the strong interaction of Mg ions with the electrodes and electrolytes are the main challenges inhibiting the development of aqueous MIBs. The main cathodes currently used in aqueous MIBs are chalcogenides, Mn-based materials, V-based materials and organic materials, including *tetra*-chloro-benzoquinone (C4Q) and poly(pyrene-4,5,9,10-tetraone) (PPTO). Xia *et al.* [196] pioneered an aqueous MIB consisting of a nickel hexacyanoferrate cathode and a polyimide anode. The aqueous electrolyte showed advantages in cyclability and rate performance compared with conventional organic electrolytes. Wang *et al.* [197] used the concentrated magnesium *bis*(trifluoromethylsulfonyl)imide $(Mg(TFSI)_2)$ electrolyte to broaden the electrochemical stability window of aqueous electrolytes to 2 V. They developed two Mg ion host materials, $Li_3V_2(PO_4)_3$ (LVP) and poly pyromellitic dianhydride, as cathode and anode electrodes,

respectively, proving that the diffusion rate of Mg ions in the LVP crystal structure in the aqueous electrolyte is better than that in non-aqueous electrolytes. Alshareef *et al.* [198] used a hydrated eutectic electrolyte to inhibit the dissolution of the organic anode by suppressing the water activity in the electrolyte, and the three-dimensional hydrogen bonding network effectively facilitated the ion transport. The full cell delivered a wide operating voltage of 2.2 V, showing a capacity of 38.1 mAh g^{-1} (based on the total mass of anode and cathode active materials) at 5 C and an average voltage of 1.38 V (Figure 13c). Although aqueous MIBs are similar to the ZIBs in many respects and massive cathode materials can be used universally, further efforts are required to improve electrode|electrolyte compatibility.

Compared to the above-mentioned divalent metals (Zn, Ca, Mg), Al possesses the highest volume-specific charge storage capacity (8,040 mAh cm^{-3}) owing to its three-electron redox property. However, the high charge density of Al^{3+} poses a huge challenge for its reversible insertion/extraction in cathode materials. Deng *et al.* [199] synthesized a spinel Al$_{2/3}$Li$_{1/3}$Mn$_2$O$_4$ anode material by an electrochemical conversion reaction using LiMn$_2$O$_4$ as the precursor, which delivered a discharge capacity of 151.8 mAh g^{-1} at 100 mA g^{-1} and a retention ratio of 64.1% after 1,000 cycles. Al anodes are prone to undergo the passivation and hydrogen side reactions due to their lower redox potential. Yu *et al.* [200] developed an oxidation-resistant and dendrite-suppressed Zn–Al alloy anode by depositing Al^{3+} on a Zn substrate (Figure 13d). The as-developed Zn–Al|aluminum trifluoromethanesulfonate (Al(OTF)$_3$)|Al$_x$MnO$_2$ cell exhibited a record-breaking rate capability (100 mAh g^{-1} at 3 A g^{-1}). Based on a prudent examination of the Al^{3+} solvation environment, Xu *et al.* [201] suggested that conventional water-in-salt strategies were ineffective for Al-based electrolytes, due to the high charge density of the Lewis acidic Al^{3+}. Efforts to improve cathode stability using higher salt concentrations of Al(OTf)$_3$ were counterproductive and decreased the overpotential for the hydrogen precipitation, resulting in inadequate electrochemical stability windows for Al stripping/plating.

Beyond the above battery systems, other types of aqueous multivalent ion-based batteries based on transition-metal ions as charge carriers, such as aqueous Mn-ion batteries [202,204], aqueous Sn-ion batteries [203,205] and aqueous Fe-ion batteries [206], have been explored in a guided and preliminary manner. As shown in Figure 13e, Niu *et al.* [202] reported two cathode materials, Mn$_{0.18}$V$_2$O$_5$·nH$_2$O (MnVO) and *tetra*-chloro-benzoquinone (4-Cl-BQ) for the reversible Mn^{2+} insertion chemistry in aqueous electrolytes. The layered MnVO cathode demonstrated fast and reversible Mn^{2+} insertion/extraction due to the large lattice spacing, thus, enabling the adequate power performance and stable cycling behavior. The Mn|4-Cl-BQ cell showed one pair of redox peaks located at 1.29/1.53 V in CV curves and a stable discharge voltage at ~1.37 V. Chao *et al.* [203] demonstrated two reversible alkaline aqueous Sn batteries, *i.e.* 1.45 V Sn–Ni with 314 Wh kg^{-1} (over 15,000 cycles) and 1.0 V Sn–air (lifespan over 1,900 h) batteries, characterized by the anti-corrosion, anti-HER and free dendrites (Figure 13f). Generally, all these aqueous multivalent-ion batteries are still in their infancy and far from practical applications, and the sluggish multivalent-ion kinetics originating from the inherent high charge density of multivalent ions as well as the interfacial issues between electrodes and electrolyte remains to be solved.

5   Summary and outlook

Rechargeable AMBs have been strongly considered as promising candidates in the stationary electricity storage due to their intrinsic safety, sustainability and low cost. In conclusion, we reviewed the recent progress of multiple types of AMBs, including aqueous alkali metal-ion batteries and multivalent metal-ion batteries. Especially, aqueous ZIBs are of extensive concern due to their high theoretical capacity and suitable redox potential of Zn metal anodes since our group first proposed the concept of neutral ZIBs in 2012. Although thousands of articles have been reported on this hot area, great efforts are still needed to overcome obstacles and promote the commercial application of AMBs. They include the following issues.

(1) Electrode materials. It is imperative for the rational design and/or modification of high-energy, electrochemically stable and cost-effective electrode materials toward practical applications. For the cathode materials, the ambiguous carrier storage mechanism remains to be clarified *via* spatially resolved and/or non–destructive *in-situ* characterization techniques, while an elaborate control of the crystalline structure and composition of intercalation-type cathode materials with short migration channels and robust structural integrity is promising to simultaneously achieve long-term cycling, high capacity and fast ion insertion kinetics; carbon coating and defect engineering have been proved to be effective approaches for further performance improvement. On the anode side, the efficient suppression of interfacial side reactions (*e.g.*, corrosion, hydrogen evolution reaction and/or dendrite formation) by the surface modification and anode structure/composition design is of key significance to realize high CE, satisfied active material utilization and long lifespan.

(2) Aqueous electrolytes. The narrow electrochemical window of aqueous electrolytes is the main cause of the low energy density of AMBs. Great progress has been made to widen the stability window of aqueous electrolytes and suppress the interfacial side reactions by developing highly

concentrated electrolytes and introducing organic co-sol-vent/passivation film-forming electrolyte additives. Fur-thermore, the design principles for wide-temperature-range electrolytes should be conducted based on their inherent advantages of non-flammability, high ionic conductivity, and cost-effectiveness. Adjusting the hydrogen bond receptor in the electrolytes by applying suitable additive/co-solvents or gelation treatment is promising to reduce the freezing point and improve the low-temperature performance, meanwhile the flame-retardant additive is highly favorable to relieve the aggravated interfacial side reactions and self-discharge issues at high temperatures.

(3) Road to the commercialization. Ultrathin separators, corrosion-resistant current collectors, low-expansion conductive additives and stable binders are highly important for the long-term operation of practical AMBs. However, these key battery components have long been overlooked in the laboratory research. In addition to these challenges, more efforts are still needed to engineer electrode materials toward commercial applications, *e.g.*, thick cathode, high tap density, low N/P ratio, and low-content conductive additives. Further, to realize the application of AMB packs in smart grids, corresponding battery protection and management systems together with the life prediction and intelligent monitoring techniques are highly required to be further developed.

Although the overall cost of AMBs may be estimated to be less than many current rechargeable battery chemistries, future cost analyses must consider both the anode (*e.g.*, Zn foil) thickness and the cathode's area capacity to realize practical optimization schemes that can be used for scaling up production. In addition, the ecological toxicity of the materials used in the batteries must also be considered, especially in the context of handling or recycling waste batteries. The use of aqueous electrolytes and non-toxic components makes it easy to integrate them with pyrometallurgical or hydrometallurgical processes that have been widely employed for the treatment of waste alkaline batteries. In conclusion, considering the rapidly growing academic and industrial interests in material updating and device engineering for AMBs, it is reasonable to expect important breakthroughs in the practical viability for applications in portable/wearable electronics, back-up power for the communication base station, large-scale energy storage station, *etc.*, in the near future.

Conflict of interest   The authors declare no conflict of interest.

1   Liu Y, Lu X, Lai F, Liu T, Shearing PR, Parkin IP, He G, Brett DJL. *Joule*, 2021, 5: 2845–2903

2   Fuldauer LI, Thacker S, Haggis RA, Fuso-Nerini F, Nicholls RJ, Hall JW. *Nat Commun*, 2022, 13: 3579

3   Kikstra JS, Vinca A, Lovat F, Boza-Kiss B, van Ruijven B, Wilson C, Rogelj J, Zakeri B, Fricko O, Riahi K. *Nat Energy*, 2021, 6: 1114–1123

4   Chang X, Zhao YM, Yuan B, Fan M, Meng Q, Guo YG, Wan LJ. *Sci China Chem*, 2023, DOI:10.1007/s11426-022-1525-3

5   Whittingham MS. *Science*, 1976, 192: 1126–1127

6   Thacker S, Adshead D, Fay M, Hallegatte S, Harvey M, Meller H, O'Regan N, Rozenberg J, Watkins G, Hall JW. *Nat Sustain*, 2019, 2: 324–331

7   Yang Z, Wang B, Chen Y, Zhou W, Li H, Zhao R, Li X, Zhang T, Bu F, Zhao Z, Li W, Chao D, Zhao D. *Natl Sci Rev*, 2023, 10: 268

8   Liang Y, Yao Y. *Nat Rev Mater*, 2023, 8: 109–122

9   Li L, Zhang Q, He B, Pan R, Wang Z, Chen M, Wang Z, Yin K, Yao Y, Wei L, Sun L. *Adv Mater*, 2022, 34: 2104327

10 Zhu K, Sun Z, Li Z, Liu P, Li H, Jiao L. *Adv Energy Mater*, 2023, 13: 2203708

11 Kurzweil P. *J Power Sources*, 2010, 195: 4424–4434

12 Zhao Y, Pohl O, Bhatt AI, Collis GE, Mahon PJ, Rüther T, Hollenkamp AF. *Sustain Chem*, 2021, 2: 167–205

13 May GJ, Davidson A, Monahov B. *J Energy Storage*, 2018, 15: 145–157

14 Shukla A. *J Power Sources*, 2001, 100: 125–148

15 Yang H, Zhang T, Chen D, Tan Y, Zhou W, Li L, Li W, Li G, Han W, Fan HJ, Chao D. *Adv Mater*, 2023, 35: 202300053

16 Scrosati B. *J Solid State Electrochem*, 2011, 15: 1623–1630

17 Shin J, Choi JW. *Adv Energy Mater*, 2020, 10: 2001386

18 Du W, Yan J, Cao C, Li CC. *Energy Storage Mater*, 2022, 52: 329–354

19 Li W, McKinnon WR, Dahn JR. *J Electrochem Soc*, 1994, 141: 2310–2316

20 Liang Y, Dong H, Aurbach D, Yao Y. *Nat Energy*, 2020, 5: 646–656

21 Zhang Z, Yang X, Li P, Wang Y, Zhao X, Safaei J, Tian H, Zhou D, Li B, Kang F, Wang G. *Adv Mater*, 2022, 34: 2206970

22 Xu C, Li B, Du H, Kang F. *Angew Chem Int Ed*, 2012, 51: 933–935

23 Li C, Wang L, Zhang J, Zhang D, Du J, Yao Y, Hong G. *Energy Storage Mater*, 2022, 44: 104–135

24 Wang F, Borodin O, Gao T, Fan X, Sun W, Han F, Faraone A, Dura JA, Xu K, Wang C. *Nat Mater*, 2018, 17: 543–549

25 Chao D, Zhou W, Xie F, Ye C, Li H, Jaroniec M, Qiao SZ. *Sci Adv*, 2020, 6: 4098

26 Xu K, Wang C. *Nat Energy*, 2016, 1: 16161

27 Suo L, Borodin O, Gao T, Olguin M, Ho J, Fan X, Luo C, Wang C, Xu K. *Science*, 2015, 350: 938–943

28 Suo L, Borodin O, Sun W, Fan X, Yang C, Wang F, Gao T, Ma Z, Schroeder M, von Cresce A, Russell SM, Armand M, Angell A, Xu K, Wang C. *Angew Chem Int Ed*, 2016, 55: 7136–7141

29 Yamada Y, Usui K, Sodeyama K, Ko S, Tateyama Y, Yamada A. *Nat Energy*, 2016, 1: 16129

30 Yang C, Chen J, Ji X, Pollard TP, Lü X, Sun CJ, Hou S, Liu Q, Liu C, Qing T, Wang Y, Borodin O, Ren Y, Xu K, Wang C. *Nature*, 2019, 569: 245–250

31 Yue J, Zhang J, Tong Y, Chen M, Liu L, Jiang L, Lv T, Hu Y, Li H, Huang X, Gu L, Feng G, Xu K, Suo L, Chen L. *Nat Chem*, 2021, 13: 1061–1069

32 Xie J, Liang Z, Lu YC. *Nat Mater*, 2020, 19: 1006–1011

33 Jaumaux P, Yang X, Zhang B, Safaei J, Tang X, Zhou D, Wang C, Wang G. *Angew Chem Int Ed*, 2021, 60: 19965–19973

34 Suo L, Borodin O, Wang Y, Rong X, Sun W, Fan X, Xu S, Schroeder MA, Cresce AV, Wang F, Yang C, Hu YS, Xu K, Wang C. *Adv Energy Mater*, 2017, 7: 1701189

35 Jiang L, Liu L, Yue J, Zhang Q, Zhou A, Borodin O, Suo L, Li H, Chen L, Xu K, Hu YS. *Adv Mater*, 2020, 32: 1904427

36 Jiang L, Lu Y, Zhao C, Liu L, Zhang J, Zhang Q, Shen X, Zhao J, Yu X, Li H, Huang X, Chen L, Hu YS. *Nat Energy*, 2019, 4: 495–503

37 Li X, Zhou Q, Yang Z, Zhou X, Qiu D, Qiu H, Huang X, Yu Y.

Energy Environ Mater, 2023, 6: 12378

38 Zhao J, Xu Z, Zhou Z, Xi S, Xia Y, Zhang Q, Huang L, Mei L, Jiang Y, Gao J, Zeng Z, Tan C. *ACS Nano*, 2021, 15: 10597–10608

39 Hou Z, Zhang T, Liu X, Xu Z, Liu J, Zhou W, Qian Y, Fan HJ, Chao D, Zhao D. *Sci Adv*, 2022, 8: 8960

40 Zhang Q, Xia K, Ma Y, Lu Y, Li L, Liang J, Chou S, Chen J. *ACS Energy Lett*, 2021, 6: 2704–2712

41 Yu L, Huang J, Wang S, Qi L, Wang S, Chen C. *Adv Mater*, 2023, 35: 2210789

42 Li C, Kingsbury R, Thind AS, Shyamsunder A, Fister TT, Klie RF, Persson KA, Nazar LF. *Nat Commun*, 2023, 14: 3067

43 Zhou L, Wang F, Yang F, Liu X, Yu Y, Zheng D, Lu X. *Angew Chem Int Ed*, 2022, 61: e202208051

44 Xie S, Li X, Li Y, Liang Q, Dong L. *Chem Record*, 2022, 22: e202200201

45 Sun W, Wang F, Hou S, Yang C, Fan X, Ma Z, Gao T, Han F, Hu R, Zhu M, Wang C. *J Am Chem Soc*, 2017, 139: 9775–9778

46 Huang Y, Mou J, Liu W, Wang X, Dong L, Kang F, Xu C. *Nano-Micro Lett*, 2019, 11: 49

47 Ye X, Han D, Jiang G, Cui C, Guo Y, Wang Y, Zhang Z, Weng Z, Yang QH. *Energy Environ Sci*, 2023, 16: 1016–1023

48 Zhao Y, Zhang P, Liang J, Xia X, Ren L, Song L, Liu W, Sun X. *Energy Storage Mater*, 2022, 47: 424–433

49 Yuan Y, Sharpe R, He K, Li C, Saray MT, Liu T, Yao W, Cheng M, Jin H, Wang S, Amine K, Shahbazian-Yassar R, Islam MS, Lu J. *Nat Sustain*, 2022, 5: 890–898

50 Pan H, Shao Y, Yan P, Cheng Y, Han KS, Nie Z, Wang C, Yang J, Li X, Bhattacharya P, Mueller KT, Liu J. *Nat Energy*, 2016, 1: 16039

51 Islam S, Alfaruqi MH, Putro DY, Park S, Kim S, Lee S, Ahmed MS, Mathew V, Sun YK, Hwang JY, Kim J. *Adv Sci*, 2021, 8: 2002636

52 Liu Z, Li L, Qin L, Guo S, Fang G, Luo Z, Liang S. *Adv Mater*, 2022, 34: 2204681

53 Wu D, Housel LM, Kim SJ, Sadique N, Quilty CD, Wu L, Tappero R, Nicholas SL, Ehrlich S, Zhu Y, Marschilok AC, Takeuchi ES, Bock DC, Takeuchi KJ. *Energy Environ Sci*, 2020, 13: 4322–4333

54 Gourley SWD, Brown R, Adams BD, Higgins D. *Joule*, 2023, DOI:10.1016/j.joule.2023.06.007

55 Zhang J, Kim JB, Zhang J, Lee GH, Chen M, Lau VW, Zhang K, Lee S, Chen CL, Jeon TY, Kwon YW, Kang YM. *J Am Chem Soc*, 2022, 144: 7929–7938

56 Zhang D, Cao J, Zhang X, Insin N, Wang S, Han J, Zhao Y, Qin J, Huang Y. *Adv Funct Mater*, 2021, 31: 2009412

57 Fang G, Zhu C, Chen M, Zhou J, Tang B, Cao X, Zheng X, Pan A, Liang S. *Adv Funct Mater*, 2019, 29: 1808375

58 Wang C, Yang H, Wang B, Ding P, Wan Y, Bao W, Li Y, Ma S, Liu Y, Lu Y, Hu H. *Nano Res*, 2023, DOI:10.1007/s12274-023-5717-8

59 Wu B, Zhang G, Yan M, Xiong T, He P, He L, Xu X, Mai L. *Small*, 2018, 14: 1703850

60 Wang C, Zeng Y, Xiao X, Wu S, Zhong G, Xu K, Wei Z, Su W, Lu X. *J Energy Chem*, 2020, 43: 182–187

61 Xu D, Li B, Wei C, He YB, Du H, Chu X, Qin X, Yang QH, Kang F. *Electrochim Acta*, 2014, 133: 254–261

62 Li H, Han C, Huang Y, Huang Y, Zhu M, Pei Z, Xue Q, Wang Z, Liu Z, Tang Z, Wang Y, Kang F, Li B, Zhi C. *Energy Environ Sci*, 2018, 11: 941–951

63 Fu Y, Wei Q, Zhang G, Wang X, Zhang J, Hu Y, Wang D, Zuin L, Zhou T, Wu Y, Sun S. *Adv Energy Mater*, 2018, 8: 1801445

64 Wu L, Dong Y. *Energy Storage Mater*, 2021, 41: 715–737

65 Tan Q, Li X, Zhang B, Chen X, Tian Y, Wan H, Zhang L, Miao L, Wang C, Gan Y, Jiang J, Wang Y, Wang H. *Adv Energy Mater*, 2020, 10: 2001050

66 Jiang B, Xu C, Wu C, Dong L, Li J, Kang F. *Electrochim Acta*, 2017, 229: 422–428

67 Kundu D, Adams BD, Duffort V, Vajargah SH, Nazar LF. *Nat Energy*, 2016, 1: 16119

68 Kim Y, Park Y, Kim M, Lee J, Kim KJ, Choi JW. *Nat Commun*, 2022, 13: 2371

69 Yan S, Abhilash KP, Tang L, Yang M, Ma Y, Xia Q, Guo Q, Xia H. *Small*, 2018, 15: 1804371

70 Wan F, Zhang L, Dai X, Wang X, Niu Z, Chen J. *Nat Commun*, 2018, 9: 1656

71 Lu Y, Zhu T, Bergh W, Stefik M, Huang K. *Angew Chem Int Ed*, 2020, 59: 17004–17011

72 Zhou M, Chen Y, Fang G, Liang S. *Energy Storage Mater*, 2021, 45: 618–646

73 Liao M, Wang J, Ye L, Sun H, Wen Y, Wang C, Sun X, Wang B, Peng H. *Angew Chem Int Ed*, 2020, 59: 2273–2278

74 Cui F, Wang D, Hu F, Yu X, Guan C, Song G, Xu F, Zhu K. *Energy Storage Mater*, 2022, 44: 197–205

75 Li Z, Ren Y, Mo L, Liu C, Hsu K, Ding Y, Zhang X, Li X, Hu L, Ji D, Cao G. *ACS Nano*, 2020, 14: 5581–5589

76 Zheng Y, Tian C, Wu Y, Li L, Tao Y, Liang L, Yu G, Sun J, Wu S, Wang F, Pang Y, Shen Z, Pan Z, Chen H, Wang J. *Energy Storage Mater*, 2022, 52: 664–674

77 Ming F, Liang H, Lei Y, Kandambeth S, Eddaoudi M, Alshareef HN. *ACS Energy Lett*, 2018, 3: 2602–2609

78 Tang B, Zhou J, Fang G, Liu F, Zhu C, Wang C, Pan A, Liang S. *J Mater Chem A*, 2019, 7: 940–945

79 Ou L, Ou H, Qin M, Liu Z, Fang G, Cao X, Liang S. *ChemSusChem*, 2022, 15: e202201184

80 Bin D, Huo W, Yuan Y, Huang J, Liu Y, Zhang Y, Dong F, Wang Y, Xia Y. *Chem*, 2020, 6: 968–984

81 Chen S, Li K, Hui KS, Zhang J. *Adv Funct Mater*, 2020, 30: 2003890

82 Xu Y, Fan G, Sun PX, Guo Y, Wang Y, Gu X, Wu L, Yu L. *Angew Chem Int Ed*, 2023, 62: e202303529

83 Zong Q, Wang QQ, Liu C, Tao D, Wang J, Zhang J, Du H, Chen J, Zhang Q, Cao G. *ACS Nano*, 2022, 16: 4588–4598

84 Wang X, Li Y, Wang S, Zhou F, Das P, Sun C, Zheng S, Wu ZS. *Adv Energy Mater*, 2020, 10: 2000081

85 Liu Y, Xiao X, Liu X, Cui LL, Gong Y. *J Mater Chem A*, 2022, 10: 912–927

86 Deng S, Yuan Z, Tie Z, Wang C, Song L, Niu Z. *Angew Chem Int Ed*, 2020, 59: 22002–22006

87 Liu C, Li R, Liu W, Shen G, Chen D. *ACS Appl Mater Interfaces*, 2021, 13: 37194–37200

88 Feng D, Lei T, Lukatskaya MR, Park J, Huang Z, Lee M, Shaw L, Chen S, Yakovenko AA, Kulkarni A, Xiao J, Fredrickson K, Tok JB, Zou X, Cui Y, Bao Z. *Nat Energy*, 2018, 3: 30–36

89 Zhang L, Chen L, Zhou X, Liu Z. *Adv Energy Mater*, 2015, 5: 1400930

90 Pu X, Jiang B, Wang X, Liu W, Dong L, Kang F, Xu C. *Nano-Micro Lett*, 2020, 12: 152

91 Hong H, Guo X, Zhu J, Wu Z, Li Q, Zhi C. *Sci China Chem*, 2023, DOI:10.1007/s11426-023-1558-2

92 Khayum MA, Ghosh M, Vijayakumar V, Halder A, Nurhuda M, Kumar S, Addicoat M, Kurungot S, Banerjee R. *Chem Sci*, 2019, 10: 8889–8894

93 Nam KW, Park SS, dos Reis R, Dravid VP, Kim H, Mirkin CA, Stoddart JF. *Nat Commun*, 2019, 10: 4948

94 Peng H, Huang S, Montes-García V, Pakulski D, Guo H, Richard F, Zhuang X, Samorì P, Ciesielski A. *Angew Chem Int Ed*, 2023, 62: 202216136

95 He Y, Liu M, Chen S, Zhang J. *Sci China Chem*, 2021, 65: 391–398

96 Wang Y, Song J, Wong WY. *Angew Chem Int Ed*, 2023, 62: e202218343

97 Lu Y, Zhang Q, Li L, Niu Z, Chen J. *Chem*, 2018, 4: 2786–2813

98 Li Z, Tan J, Wang Y, Gao C, Wang Y, Ye M, Shen J. *Energy Environ Sci*, 2023, 16: 2398–2431

99 Qiu X, Xu J, Zhou K, Huang X, Liao M, Cao Y, Zhou G, Wei P, Wang Y. *Angew Chem Int Ed*, 2023, 62: e202304036

100 Yan L, Zhu Q, Qi Y, Xu J, Peng Y, Shu J, Ma J, Wang Y. *Angew Chem Int Ed*, 2022, 61: e202211107

101 Wang X, Liu Y, Wei Z, Hong J, Liang H, Song M, Zhou Y, Huang X. *Adv Mater*, 2022, 34: 2206812

102 Kundu D, Oberholzer P, Glaros C, Bouzid A, Tervoort E, Pasquarello A, Niederberger M. *Chem Mater*, 2018, 30: 3874–3881

103 Lin Z, Shi HY, Lin L, Yang X, Wu W, Sun X. *Nat Commun*, 2021, 12: 4424

104 Guo Z, Ma Y, Dong X, Huang J, Wang Y, Xia Y. *Angew Chem Int Ed*, 2018, 57: 11737–11741

105 Tie Z, Liu L, Deng S, Zhao D, Niu Z. *Angew Chem Int Ed*, 2020, 59: 4920–4924

106 Ye Z, Xie S, Cao Z, Wang L, Xu D, Zhang H, Matz J, Dong P, Fang H, Shen J, Ye M. *Energy Storage Mater*, 2021, 37: 378–386

107 Ma X, Cao X, Yao M, Shan L, Shi X, Fang G, Pan A, Lu B, Zhou J, Liang S. *Adv Mater*, 2022, 34: 2105452

108 Yang M, Wang Y, Ma D, Zhu J, Mi H, Zhang Z, Wu B, Zeng L, Chen M, Chen J, Zhang P. *Angew Chem Int Ed*, 2023, 62: e202304400

109 Liu W, Hao J, Xu C, Mou J, Dong L, Jiang F, Kang Z, Wu J, Jiang B, Kang F. *Chem Commun*, 2017, 53: 6872–6874

110 Shi J, Hou Y, Liu Z, Zheng Y, Wen L, Su J, Li L, Liu N, Zhang Z, Gao Y. *Nano Energy*, 2022, 91: 106651

111 Chao D, Qiao SZ. *Joule*, 2020, 4: 1846–1851

112 Song M, Tan H, Chao D, Fan HJ. *Adv Funct Mater*, 2018, 28: 1802564

113 Hao J, Li B, Li X, Zeng X, Zhang S, Yang F, Liu S, Li D, Wu C, Guo Z. *Adv Mater*, 2020, 32: 2003021

114 He H, Tong H, Song X, Song X, Liu J. *J Mater Chem A*, 2020, 8: 7836–7846

115 Kim JY, Liu G, Shim GY, Kim H, Lee JK. *Adv Funct Mater*, 2020, 30: 2004210

116 Liang P, Yi J, Liu X, Wu K, Wang Z, Cui J, Liu Y, Wang Y, Xia Y, Zhang J. *Adv Funct Mater*, 2020, 30: 1908528

117 So S, Ahn YN, Ko J, Kim IT, Hur J. *Energy Storage Mater*, 2022, 52: 40–51

118 Xing Z, Sun Y, Xie X, Tang Y, Xu G, Han J, Lu B, Liang S, Chen G, Zhou J. *Angew Chem Int Ed*, 2023, 62: 202215324

119 Yu J, Jia X, Peng J, Wang T, Feng H, Meng B, Zhao JK, Yang N. *J Electrochem Soc*, 2023, 170: 020504

120 Zhou Y, Xie S, Li Y, Zheng Z, Dong L. *J Colloid Interface Sci*, 2023, 630: 676–684

121 Zhang N, Huang S, Yuan Z, Zhu J, Zhao Z, Niu Z. *Angew Chem Int Ed*, 2021, 60: 2861–2865

122 Han D, Wu S, Zhang S, Deng Y, Cui C, Zhang L, Long Y, Li H, Tao Y, Weng Z, Yang Q-, Kang F. *Small*, 2020, 16: 2001736

123 Li S, Fu J, Miao G, Wang S, Zhao W, Wu Z, Zhang Y, Yang X. *Adv Mater*, 2021, 33: 2008424

124 Wang Y, Chen Y, Liu W, Ni X, Qing P, Zhao Q, Wei W, Ji X, Ma J, Chen L. *J Mater Chem A*, 2021, 9: 8452–8461

125 Xie S, Li Y, Li X, Zhou Y, Dang Z, Rong J, Dong L. *Nano-Micro Lett*, 2021, 14: 39

126 Hao J, Li X, Zhang S, Yang F, Zeng X, Zhang S, Bo G, Wang C, Guo Z. *Adv Funct Mater*, 2020, 30: 2001263

127 Yuksel R, Buyukcakir O, Seong WK, Ruoff RS. *Adv Energy Mater*, 2020, 10: 1904215

128 Liu H, Wang JG, Hua W, Ren L, Sun H, Hou Z, Huyan Y, Cao Y, Wei C, Kang F. *Energy Environ Sci*, 2022, 15: 1872–1881

129 Zhao R, Dong X, Liang P, Li H, Zhang T, Zhou W, Wang B, Yang Z, Wang X, Wang L, Sun Z, Bu F, Zhao Z, Li W, Zhao D, Chao D. *Adv Mater*, 2023, 35: 2209288

130 Yang Y, Xiao J, Cai J, Wang G, Du W, Zhang Y, Lu X, Li CC. *Adv Funct Mater*, 2020, 31: 2005092

131 Zhou LF, Du T, Li JY, Wang YS, Gong H, Yang QR, Chen H, Luo WB, Wang JZ. *Mater Horiz*, 2022, 9: 2722–2751

132 Huang C, Zhao X, Hao Y, Yang Y, Qian Y, Chang G, Zhang Y, Tang Q, Hu A, Chen X. *Adv Funct Mater*, 2022, 32: 2112091

133 Peng H, Fang Y, Wang J, Ruan P, Tang Y, Lu B, Cao X, Liang S, Zhou J. *Matter*, 2022, 5: 4363–4378

134 Wang SB, Ran Q, Yao RQ, Shi H, Wen Z, Zhao M, Lang XY, Jiang Q. *Nat Commun*, 2020, 11: 1634

135 Wang L, Huang W, Guo W, Guo ZH, Chang C, Gao L, Pu X. *Adv*

136 Tian H, Feng G, Wang Q, Li Z, Zhang W, Lucero M, Feng Z, Wang ZL, Zhang Y, Zhen C, Gu M, Shan X, Yang Y. *Nat Commun*, 2022, 13: 7922

137 Chai Y, Xie X, He Z, Guo G, Wang P, Xing Z, Lu B, Liang S, Tang Y, Zhou J. *Chem Sci*, 2022, 13: 11656–11665

138 Huang Y, Chang Z, Liu W, Huang W, Dong L, Kang F, Xu C. *Chem Eng J*, 2022, 431: 133902

139 Tian Y, An Y, Wei C, Xi B, Xiong S, Feng J, Qian Y. *Adv Energy Mater*, 2020, 11: 2002529

140 Chae MS, Heo JW, Lim SC, Hong ST. *Inorg Chem*, 2016, 55: 3294–3301

141 Li W, Wang K, Cheng S, Jiang K. *Adv Energy Mater*, 2019, 9: 1900993

142 Wang B, Yan J, Zhang Y, Ye M, Yang Y, Li CC. *Adv Funct Mater*, 2021, 31: 2102827

143 Hou Z, Zhang X, Chen J, Qian Y, Chen LF, Lee PS. *Adv Energy Mater*, 2022, 12: 2104053

144 Chen Z, Li C, Yang Q, Wang D, Li X, Huang Z, Liang G, Chen A, Zhi C. *Adv Mater*, 2021, 33: 2105426

145 Li W, Ma Y, Li P, Jing X, Jiang K, Wang D. *Adv Energy Mater*, 2021, 11: 2102607

146 Zhu Y, Cui Y, Alshareef HN. *Nano Lett*, 2021, 21: 1446–1453

147 Wang C, Wang D, Lv D, Peng H, Song X, Yang J, Qian Y. *Adv Energy Mater*, 2023, 13: 2204388

148 Zheng X, Liu Z, Sun J, Luo R, Xu K, Si M, Kang J, Yuan Y, Liu S, Ahmad T, Jiang T, Chen N, Wang M, Xu Y, Chuai M, Zhu Z, Peng Q, Meng Y, Zhang K, Wang W, Chen W. *Nat Commun*, 2023, 14: 76

149 Cao L, Li D, Pollard T, Deng T, Zhang B, Yang C, Chen L, Vatamanu J, Hu E, Hourwitz MJ, Ma L, Ding M, Li Q, Hou S, Gaskell K, Fourkas JT, Yang XQ, Xu K, Borodin O, Wang C. *Nat Nanotechnol*, 2021, 16: 902–910

150 An Y, Tian Y, Zhang K, Liu Y, Liu C, Xiong S, Feng J, Qian Y. *Adv Funct Mater*, 2021, 31: 2101886

151 Zhang Q, Ma Y, Lu Y, Zhou X, Lin L, Li L, Yan Z, Zhao Q, Zhang K, Chen J. *Angew Chem Int Ed*, 2021, 60: 23357–23364

152 Ming F, Zhu Y, Huang G, Emwas AH, Liang H, Cui Y, Alshareef HN. *J Am Chem Soc*, 2022, 144: 7160–7170

153 Qin Y, Liu P, Zhang Q, Wang Q, Sun D, Tang Y, Ren Y, Wang H. *Small*, 2020, 16: 2003106

154 Wang Z, Dong L, Huang W, Jia H, Zhao Q, Wang Y, Fei B, Pan F. *Nano-Micro Lett*, 2021, 13: 73

155 Song Y, Ruan P, Mao C, Chang Y, Wang L, Dai L, Zhou P, Lu B, Zhou J, He Z. *Nano-Micro Lett*, 2022, 14: 218

156 Zhang X, Li J, Qi K, Yang Y, Liu D, Wang T, Liang S, Lu B, Zhu Y, Zhou J. *Adv Mater*, 2022, 34: 2205175

157 Liu Y, Liu S, Xie X, Li Z, Wang P, Lu B, Liang S, Tang Y, Zhou J. *InfoMat*, 2023, 5: 12374

158 Zhou W, Chen M, Tian Q, Chen J, Xu X, Wong CP. *Energy Storage Mater*, 2022, 44: 57–65

159 Liang Y, Ma D, Zhao N, Wang Y, Yang M, Ruan J, Yang G, Mi H, He C, Zhang P. *Adv Funct Mater*, 2022, 32: 2112936

160 Li C, Sun Z, Yang T, Yu L, Wei N, Tian Z, Cai J, Lv J, Shao Y, Rümmeli MH, Sun J, Liu Z. *Adv Mater*, 2020, 32: 2003425

161 Cao J, Zhang D, Gu C, Zhang X, Okhawilai M, Wang S, Han J, Qin J, Huang Y. *Nano Energy*, 2021, 89: 106322

162 Cao J, Zhang D, Gu C, Wang X, Wang S, Zhang X, Qin J, Wu ZS. *Adv Energy Mater*, 2021, 11: 2101299

163 Li Y, Peng X, Li X, Duan H, Xie S, Dong L, Kang F. *Adv Mater*, 2023, 35: 2300019

164 Arnot DJ, Lim MB, Bell NS, Schorr NB, Hill RC, Meyer A, Cheng YT, Lambert TN. *Adv Energy Mater*, 2021, 11: 2101594

165 Hou Z, Gao Y, Tan H, Zhang B. *Nat Commun*, 2021, 12: 3083

166 Fu J, Wang H, Xiao P, Zeng C, Sun Q, Li H. *Energy Storage Mater*, 2022, 48: 191–191.f6

167 Lee BS, Cui S, Xing X, Liu H, Yue X, Petrova V, Lim HD, Chen R, Liu P. *ACS Appl Mater Interfaces*, 2018, 10: 38928–38935

168 Fang Y, Xie X, Zhang B, Chai Y, Lu B, Liu M, Zhou J, Liang S. *Adv Funct Mater*, 2021, 32: 2109671

169 Yao L, Hou C, Liu M, Chen H, Zhao Q, Zhao Y, Wang Y, Liu L, Yin ZW, Qiu J, Li S, Qin R, Pan F. *Adv Funct Mater*, 2022, 33: 2209301

170 Zhang Y, Li X, Fan L, Shuai Y, Zhang N. *Cell Rep Phys Sci*, 2022, 3: 100824

171 Huang C, Zhao X, Hao Y, Yang Y, Qian Y, Chang G, Zhang Y, Tang Q, Hu A, Chen X. *Energy Environ Sci*, 2023, 16: 1721–1731

172 Huang C, Huang F, Zhao X, Hao Y, Yang Y, Qian Y, Chang G, Zhang Y, Tang Q, Hu A, Chen X. *Adv Funct Mater*, 2022, 33: 2210197

173 Huang C, Zhao X, Hao Y, Yang Y, Qian Y, Chang G, Zhang Y, Tang Q, Hu A, Chen X. *Small*, 2022, 18: 2203674

174 Pan Y, Liu Z, Liu S, Qin L, Yang Y, Zhou M, Sun Y, Cao X, Liang S, Fang G. *Adv Energy Mater*, 2023, 13: 2203766

175 Chu Y, Zhang S, Wu S, Hu Z, Cui G, Luo J. *Energy Environ Sci*, 2021, 14: 3609–3620

176 Zeng X, Mao J, Hao J, Liu J, Liu S, Wang Z, Wang Y, Zhang S, Zheng T, Liu J, Rao P, Guo Z. *Adv Mater*, 2021, 33: 2007416

177 Bayaguud A, Luo X, Fu Y, Zhu C. *ACS Energy Lett*, 2020, 5: 3012–3020

178 Zhang SJ, Hao J, Luo D, Zhang PF, Zhang B, Davey K, Lin Z, Qiao SZ. *Adv Energy Mater*, 2021, 11: 2102010

179 Xu J, Lv W, Yang W, Jin Y, Jin Q, Sun B, Zhang Z, Wang T, Zheng L, Shi X, Sun B, Wang G. *ACS Nano*, 2022, 16: 11392–11404

180 Han D, Cui C, Zhang K, Wang Z, Gao J, Guo Y, Zhang Z, Wu S, Yin L, Weng Z, Kang F, Yang QH. *Nat Sustain*, 2021, 5: 205–213

181 Sun P, Ma L, Zhou W, Qiu M, Wang Z, Chao D, Mai W. *Angew Chem Int Ed*, 2021, 60: 18247–18255

182 Wang B, Zheng R, Yang W, Han X, Hou C, Zhang Q, Li Y, Li K, Wang H. *Adv Funct Mater*, 2022, 32: 2112693

183 Wei T, Ren Y, Wang Y, Mo L', Li Z, Zhang H, Hu L, Cao G. *ACS Nano*, 2023, 17: 3765–3775

184 Liu S, Mao J, Pang WK, Vongsvivut J, Zeng X, Thomsen L, Wang Y, Liu J, Li D, Guo Z. *Adv Funct Mater*, 2021, 31: 2104281

185 Zou P, Lin R, Pollard TP, Yao L, Hu E, Zhang R, He Y, Wang C, West WC, Ma L, Borodin O, Xu K, Yang XQ, Xin HL. *Nano Lett*, 2022, 22: 7535–7544

186 Wang Y, Wang Z, Pang WK, Lie W, Yuwono JA, Liang G, Liu S, Angelo AMD, Deng J, Fan Y, Davey K, Li B, Guo Z. *Nat Commun*, 2023, 14: 2720

187 Yu X, Li Z, Wu X, Zhang H, Zhao Q, Liang H, Wang H, Chao D, Wang F, Qiao Y, Zhou H, Sun SG. *Joule*, 2023, 7: 1145–1175

188 Jia X, Liu C, Neale ZG, Yang J, Cao G. *Chem Rev*, 2020, 120: 7795–7866

189 Liu Y, Zhao W, Pan Z, Fan Z, Zhang M, Zhao X, Chen J, Yang X. *Angew Chem Int Ed*, 2023, 62: e202302617

190 Pan Z, Liu X, Yang J, Li X, Liu Z, Loh XJ, Wang J. *Adv Energy Mater*, 2021, 11: 2100608

191 Qiu S, Xu Y, Wu X, Ji X. *Electrochem Energy Rev*, 2022, 5: 242–262

192 Adil M, Sarkar A, Roy A, Panda MR, Nagendra A, Mitra S. *ACS Appl Mater Interfaces*, 2020, 12: 11489–11503

193 Li R, Yu J, Chen F, Su Y, Chan KC, Xu ZL. *Adv Funct Mater*, 2023, 33: 202214304

194 Wang P, Wang H, Chen Z, Wu J, Luo J, Huang Y. *Nano Res*, 2022, 15: 701–708

195 Gheytani S, Liang Y, Wu F, Jing Y, Dong H, Rao KK, Chi X, Fang F, Yao Y. *Adv Sci*, 2017, 4: 1700465

196 Chen L, Bao JL, Dong X, Truhlar DG, Wang Y, Wang C, Xia Y. *ACS Energy Lett*, 2017, 2: 1115–1121

197 Wang F, Fan X, Gao T, Sun W, Ma Z, Yang C, Han F, Xu K, Wang C. *ACS Cent Sci*, 2017, 3: 1121–1128

198 Zhu Y, Guo X, Lei Y, Wang W, Emwas AH, Yuan Y, He Y, Alshareef HN. *Energy Environ Sci*, 2022, 15: 1282–1292

199 Li R, Xu C, Wu X, Zhang J, Yuan X, Wang F, Yao Q, Sadeeq (Jie Tang) Balogun M, Lu Z, Deng J. *Energy Storage Mater*, 2022, 53: 514–522

200 Yan C, Lv C, Wang L, Cui W, Zhang L, Dinh KN, Tan H, Wu C, Wu T, Ren Y, Chen J, Liu Z, Srinivasan M, Rui X, Yan Q, Yu G. *J Am Chem Soc*, 2020, 142: 15295–15304

201 Pastel GR, Chen Y, Pollard TP, Schroeder MA, Bowden ME, Zheng A, Hahn NT, Ma L, Murugesan V, Ho J, Garaga M, Borodin O, Mueller K, Greenbaum S, Xu K. *Energy Environ Sci*, 2022, 15: 2460–2469

202 Bi S, Zhang Y, Deng S, Tie Z, Niu Z. *Angew Chem Int Ed*, 2022, 61: e202200809

203 Zhou W, Song M, Liang P, Li X, Liu X, Li H, Zhang T, Wang B, Zhao R, Zhao Z, Li W, Zhao D, Chao D. *J Am Chem Soc*, 2023, 145: 10880–10889

204 Wei L, Zeng L, Wu MC, Jiang HR, Zhao TS. *J Power Sources*, 2019, 423: 203–210

205 Zhang H, Xu D, Yang F, Xie J, Liu Q, Liu DJ, Zhang M, Lu X, Meng YS. *Joule*, 2023, 7: 971–985

206 Xu Y, Wu X, Sandstrom SK, Hong JJ, Jiang H, Chen X, Ji X. *Adv Mater*, 2021, 33: 2105234